Ore Geology Reviews 80 (2017) 1191–1205

Contents lists available at ScienceDirect

Ore Geology Reviews

journal homepage: www.elsevier.com/locate/oregeorev

Trace elements of magnetite and iron isotopes of the Zankan iron deposit, westernmost Kunlun, China: A case study of seafloor hydrothermal iron deposits

Zhen-Ju Zhou [a,b], Hao-Shu Tang [c], Yan-Jing Chen [b,*], Zheng-Le Chen [a]

[a] Institute of Geomechanics, Chinese Academy of Geological Sciences, Beijing 100081, China
[b] Key Laboratory of Orogen and Crustal Evolution, Peking University, Beijing 100871, China
[c] State Key Laboratory of Ore Deposit Geochemistry, Institute of Geochemistry, Chinese Academy of Sciences, 46 Guanshui Road, Guiyang 550002, China

ARTICLE INFO

Article history:
Received 28 February 2016
Received in revised form 14 September 2016
Accepted 15 September 2016
Available online 16 September 2016

Keywords:
Magnetite
Trace element
Fe isotope
Zankan iron deposit
West Kunlun Orogen

ABSTRACT

The large Zankan iron deposit is hosted in the pre-Devonian Bulunkuole metamorphic complex within the Taxkorgan terrane, West Kunlun Orogen, southwestern China. The deposit is unique for its mineral association of magnetite, pyrite and anhydrite in variable proportions, forming disseminations, banded and massive ores. Magnetite grains from the ores show variable contents of many elements, such as Mg (182–1167 ppm), Al (198–2691 ppm), Ti (898–1677 ppm), V (112–8468 ppm), Mn (821–4695 ppm), Co (7–26 ppm), Ni (1–29 ppm), Zn (5–45 ppm), and Ga (20–62 ppm). The high Al, Ti and V contents are interpreted to result from relatively reduced, Al–Ti-rich seafloor hydrothermal activities. The magnetite coexisting with sulfide has lower Co concentrations (7.8–13 ppm) than those not coexisting with sulfides (Co = 22–26 ppm). Compositional variations of magnetite possibly related to oxygen fugacity, temperature and coexisting minerals. The δ^{56}Fe values in magnetite range from −0.3 to 0.5‰, suggesting a changing hydrothermal precipitation environment. The Fe isotope fractionation between pyrite and magnetite ($\Delta\delta^{57}Fe_{py\text{-}mag}$) range 0.2–1.1‰, implying a high-temperature crystallization (≥236 °C). The δ^{56}Fe ratios in pyrite range 0.6–0.8‰, higher than the coexisting magnetite. Such a negligible variation of positive δ^{56}Fe values indicates that the pyrite possibly originated from a slow precipitation or a transformation from FeS (mackinawite), which was induced by the rise of atmospheric oxygen at ~0.6 Ga. Integrating the data obtained from the studies including regional geology, ore geology, magnetite composition and Fe isotope geochemistry, we conclude that the Zankan Fe deposit was formed from an Early Cambrian seafloor hydrothermal system developed in a volcanic arc caused by southward subduction of Proto-Tethyan plate.

1. Introduction

Magnetite, a robust mineral in sediments, can survive mechanical and chemical processes, such as erosion, transportation and metamorphism, and also occurs widespread in various hydrothermal ore deposits, such as volcanogenic massive sulfide (VMS), banded iron formations (BIFs), veined Ag-Pb-Zn and skarn deposits (Singoyi et al., 2006; Dupuis and Beaudoin, 2011; Dare et al., 2012). It contains numerous discriminator trace elements, such as Mg, Al, Ti, V, Cr, Mn, Zn, Ni, Co and Ga, which show systematic variations in a variety of geological settings and formation conditions. Thus, chemical compositions of magnetite play an important role in investigating the types of mineral deposits and ore-forming processes (Müller et al., 2003; Beaudoin and Dupuis, 2009; Rusk et al., 2009; Dupuis and Beaudoin, 2011; Dare et al., 2012; Nadoll et al., 2012, 2014; Huang et al., 2013, 2015; Chen et al., 2015; Chung et al., 2015). Furthermore, as Fe is the main ore-forming element in iron deposits, Fe isotope analysis offers insights into the nature and source of fluids (Zhu et al., 2000, 2001; Dauphas et al., 2004; Rouxel et al., 2005; Dauphas and Rouxel, 2006; Johnson et al., 2008; Fabre et al., 2011; Yoshiya et al., 2012; Li et al., 2013; Sun et al., 2013; Hou et al., 2014).

The recently discovered Taxkorgan iron belt contains more than ten iron deposits, with a total resource of 1.556 Bt Fe, with average grades of 28–60% TFe (Dong et al., 2011, 2012; Feng et al., 2011; Yan et al., 2012a, 2012b). The belt lies at the junction of the West Kunlun Orogen and Pamir Plateau, southwestern China (Fig. 1A and B). Unlike Precambrian BIFs (banded iron formations), the deposits in the Taxkorgan iron belt were formed during the Early Paleozoic (ca. 540–510 Ma), composed of magnetite, pyrite and anhydrite with different ratios. Because of the economic importance and unique mineralogical association, the ages and genesis of the deposits and their host rocks were investigated by many researchers (e.g., Chen, 2012; Yan et al., 2012a, 2012b; Yang, 2013; Ren et al., 2013; Dong et al., 2016), and are still debated. A

* Corresponding author.
E-mail addresses: gigyjchen@126.com, yjchen@pku.edu.cn (Y.-J. Chen).

http://dx.doi.org/10.1016/j.oregeorev.2016.09.020
0169-1368/

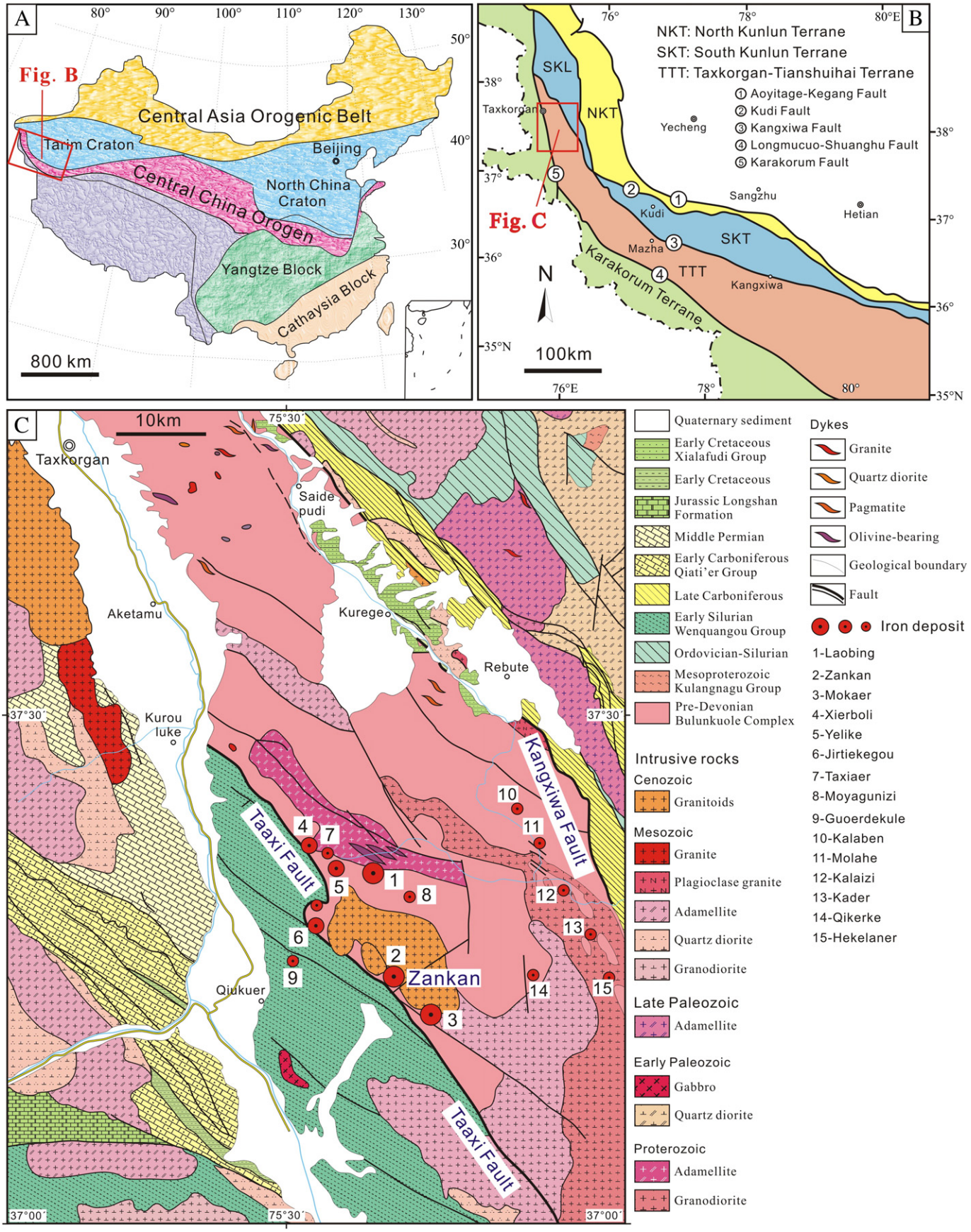

Fig. 1. (A) Tectonic subdivisions of China, showing the location of the Western Kunlun Orogen; (B) tectonic subdivision of the Western Kunlun Orogen, showing the location of the Taxkorgan iron field; (C) simplified geological map of the Taxkorgan iron belt. Modified after Ji et al. (2011) and Yan et al. (2012b).

group of researcher proposed that the deposits were metamorphosed sedimentary-type or BIF type (e.g., Chen et al., 2011, 2013; Feng et al., 2011; Qian et al., 2014); another group (e.g., Chen, 2012, 2013; Yan et al., 2012a, 2012b; Hu, 2014), in contrast, considered the deposits were related to submarine volcanism or volcanogenic hydrothermal process.

In the Taxkorgan iron belt, the Zankan iron deposit is the largest in tonnage with high ore grades, and is a typically representative mine in ore geology and geological context, and thus provides a window into ore genesis and ore-forming processes. In this paper, we present the results of in-situ trace elements of magnetite and Fe isotopes of magnetite and pyrite from Zankan iron deposit, and clarify the nature and source of the ore-fluid. We also attempt to discuss possible factors controlling the compositions of magnetite from Zankan deposit, and constrain its genetic type.

2. Regional geology

The Pamir-West Kunlun-Altun mountains (Pan and Wang, 1994; Xiao et al., 2000; Jiang et al., 2013), forming the southern margin of the Tarim Basin, eastwardly connect with the East Kunlun (Zheng et al., 2016), Qinling (Chen and Santosh, 2014; Mao et al., 2014; Li et al., 2015) and Dabie Shan (Wang et al., 2014; Mi et al., 2015), constituting the huge Central China Orogenic Belt (CCOB; Chen et al., 2014). The CCOB evolved from the northernmost Paleo-Tethys and took shape through Early Mesozoic continental collision between a North China-Tarim continent and the segments separated from Gondwana Land, after a long-time multistage subduction-related accretion and terrane amalgamation (Chen and Santosh, 2014; Zhou et al., 2014a, 2014b, 2015, 2016) (Fig. 1A).

The West Kunlun Orogen is bounded by the Aoyitage-Kegang Fault to the north and the Longmucuo-Shuanghu (or Karakorum) Fault to the south (Fig. 1B). It includes three tectonic units, from north to south, the Northern Kunlun Terrane (NKT), the Southern Kunlun Terrane (SKT), and the Taxkorgan-Tianshuihai Terrane (TTT), with the Kudi and Mazar-Kangxiwa faults being their boundaries, respectively (Fig. 1B; Xiao et al., 2005a; Yang et al., 2010).

The Taxkorgan terrane is located in the West Kunlun Orogen (Fig. 1B), bounded by the Kangxiwa Fault to the north and the Taaxi Fault (one fault of the Karakorum fault zone) to the south (Fig. 1C). The dominant lithologies in this area are pre-Devonian Bulunkuole Complex and Early Cretaceous Xialafudi Group. The Bulunkuole Complex, consists mainly of biotite plagioclase gneisses, plagioclase-amphibole gneiss, biotite quartz schists, sillimanite-garnet schists, magnetite quartzite, metamorphic siltstones, marbles and plagioclase amphibole schists. These rocks have been generally metamorphosed to greenschist to amphibolite facies. However, the sedimentation age of these rocks is still controversial, with isotope ages ranging from ca. 500 to 2700 Ma (e.g., Sun et al., 2003; Zhang et al., 2007; Ji et al., 2011; Yan et al., 2012a, 2012b). The Xialafudi Group, unconformably overlying the Bulunkuole Complex, is composed of micritic limestones, siltstones, conglomerates, sandstones, and shales, deposited on a lacustrine delta. The Bulunkuole Complex is separated from the Early Silurian Wenquangou Group by the Taaxi Fault to the south, and from the Late Carboniferous clastic sediments by the Kangxiwa Fault to the north, respectively (Fig. 1C). The Early Silurian Wenquangou Group comprises clastic sediments, including pelitic siltstone, mudstone, quartz sandstone, and minor conglomerate, and carbonate intercalations. The Late Carboniferous clastic sediments consist mainly of silty mudstones, micritic limestones, mudstones, limestones and siliceous rocks. The Taxkorgan terrane was intruded by the Proterozoic granodiorite and adamellite, followed by Mesozoic quartz diorite, adamellite and plagioclase granite, and the Cenozoic syenogranite and syenite (Fig. 1C).

More than 10 iron deposits have been discovered in the Taxkorgan terrane. They are hosted in the Bulunkuole Complex, except for the Guoerkule deposit which is a small-sized deposit hosted in the Early Wenquangou Group (Fig. 1C). Yan et al. (2012a, 2012b) and Yang (2013) constrained the mineralization at Laobing and Ziluoyi iron deposits to have occurred at 526 ± 5.0 Ma and ca. 500 Ma, respectively, through zircon LA-ICP-MS U–Pb dating for biotite-quartz schists. Recently, Lin (2015) and Dong et al. (2016) obtained the zircon LA-ICP-MS U–Pb ages of 527.4 ± 9.0–536.8 ± 3.4 Ma for volcanic rocks from the Zankan deposit. Thus it is accepted that the iron mineralization in Taxkorgan terrane mainly occurred in Early Cambrian, coeval with the initiation of the Early Paleozoic Andean-type magmatic arc (540–435 Ma) in the West Kunlun Orogen (Xu et al., 1994; Xiao et al., 2005a; Liao et al., 2010; Jia et al., 2013). The Taxkorgan iron belt was intensively involved in the southward subduction of Proto-Tethyan plate beneath the SKT and TTT during the Early Paleozoic.

3. Deposit geology

The Zankan iron deposit is located in the northern part of the Taxkorgan terrane (Fig. 1C). It has a proven reserve of 1.46×10^8 t Fe with an average grade of 28.3–58.8%, plus an inferred resource of 1.8×10^8 t Fe (Dong et al., 2011; Feng et al., 2011). The main lithostratigraphic units in the Zankan orefield are the Bulunkuole Complex and Early Silurian Wenquangou Group (Fig. 2). The Bulunkuole Complex in the orefield mainly includes biotite-quartz schists, plagioclase-amphibole schists, and amphibole-quartz schists, intercalated with gypsum layers, which was metamorphosed to greenschist facies (locally up to amphibolite facies). The Early Silurian Wenquangou Group, unconformably overlying the Bulunkuole Complex, mainly consists of quartzite, quartz sandstone and marble.

The orebodies at Zankan are hosted in the Bulunkuole Complex, and spatially associated with the volcanic rocks. The volcanic rocks are composed of metamorphosed dacite and andesite, forming in Early Cambrian continental arc setting (Lin, 2015; Dong et al., 2016). The volcanic rocks in the hanging wall (Fig. 2) are conformable with iron orebodies, and locally altered into iron ores. They show porphyritic texture, with 20–40 vol.% phenocrysts composed of hornblende, plagioclase and quartz. The groundmass is composed of quartz, plagioclase and biotite. Accessory minerals include apatite, magnetite and zircon. Zircon grains from two samples of volcanic rocks collected from the hanging wall and the contact zone yield LA-ICP-MS U–Pb ages of 536.4 ± 4.0 Ma and 536.8 ± 3.4 Ma, respectively (Dong et al., 2016). Lin (2015) reported the zircon U–Pb ages of 533 ± 10 Ma and 527.4 ± 9.0 Ma for the subvolcanic rocks intruding the footwall of the iron orebodies (Fig. 2).

Five orebodies have been recognized in the Zankan deposit. No. 1 orebody is 2493-m long, and 10–21-m thick, accounting for 72% of the total reserve of the Zankan deposit. It strikes in the direction of 30–40°, and dips to NE with angle of 27–70°. The No. 3 orebody, the second largest one, is >1000 m long, 8.8–14-m thick, and strikes in direction of 19–41°, dips to NE with angle of 6–57°. The other orebodies are generally >400 m long, ~10 m thick. Orebodies are shaped as beds and lens, and generally share the same occurring state with their host rocks, showing the nature of stratiform or stratabound deposits (Figs. 2 and 3).

The ores are massive, disseminated, and banded in texture (Fig. 4). Three types of ores have similar ore mineral assemblages dominated by magnetite, pyrite, and minor chalcopyrite and pyrrhotite. Gangue minerals mainly consist of quartz, anhydrite, plagioclase, hornblende, biotite, muscovite, calcite, and minor sphene and apatite. Massive ores commonly have subhedral to anherdral magnetite associated with pyrite and anhydrite (Fig. 5A-C). Magnetite is generally 0.06 to 0.5 mm in diameter, often present as thin bands. Pyrite occurs as disseminations and continuous to discontinuous laminae/bands (Fig. 4A-C). Banded ore shows structures of interbedded magnetite, pyrite and anhydrite (Fig. 4E). Magnetite occurs as euhedral to subhedral crystals (Fig. 5D). Disseminated ores have a mineral assemblage of anhedral magnetite, pyrite and pyrrhotite (Figs. 4F and 5E). Pyrite occurs as subhedral to anhedral and is locally replaced by chalcopyrite (Fig. 5F). Pyrrhotite is subhedral to anhedral. Nine samples, including massive (ZKA3-1, ZKPM6-2, ZKA3-1M, ZK10-526, ZK10-359, and ZK10-306), banded

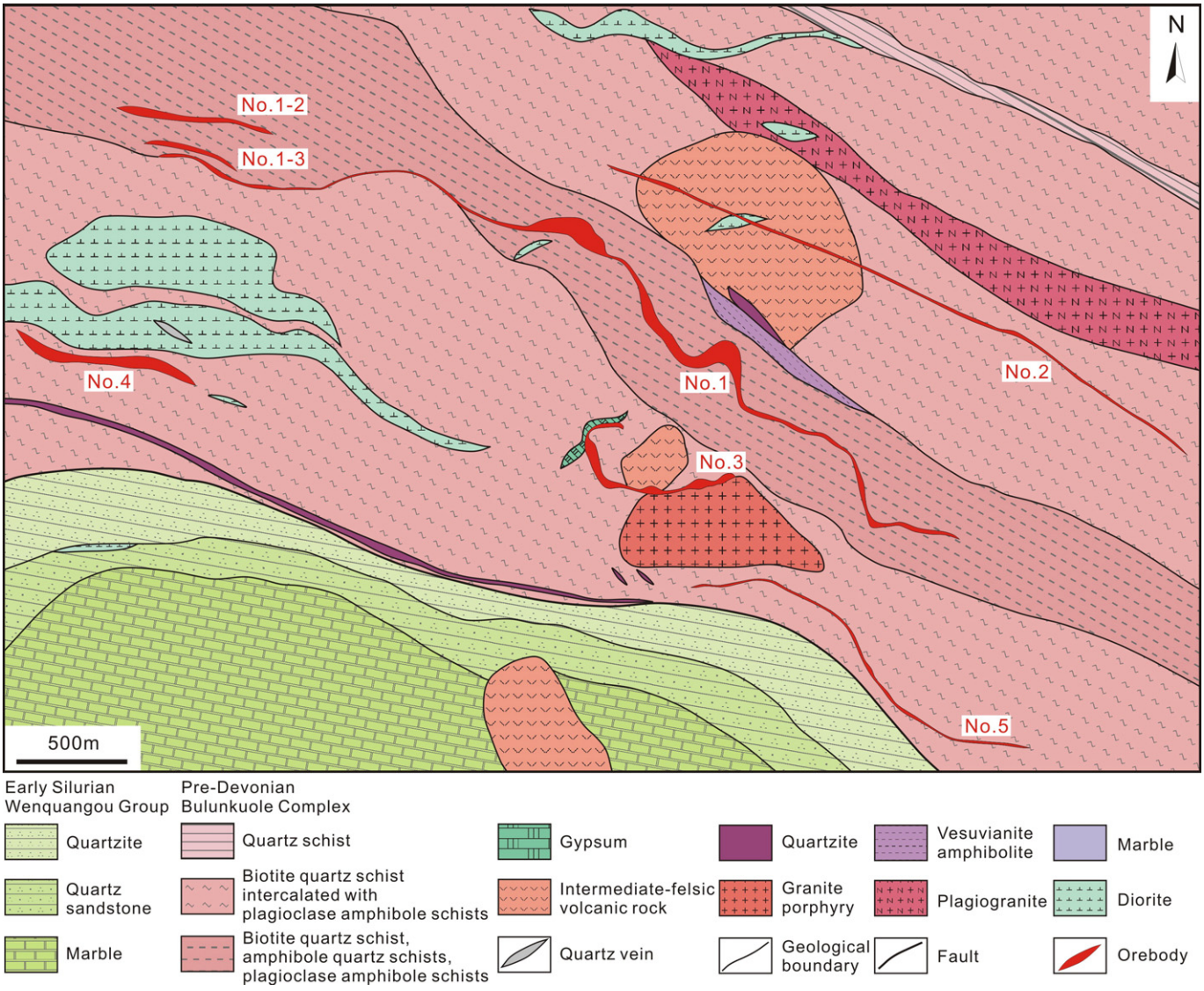

Fig. 2. Simplified geological map of the Zankan iron deposit.

(ZKA1-2) and disseminated (ZK10-371 and ZK10-531) ores, are selected for further detection in this study (Figs. 4 and 5).

4. Analytical methods

4.1. Chemical composition of magnetite

Trace elements of magnetite were determined by a Coherent GeoLasPro 193 nm Laser Ablation system coupled with an Agilent 7700× ICP-MS at the State Key Laboratory of Ore Deposit Geochemistry, Institute of Geochemistry, Chinese Academy of Sciences, Guiyang, China. Detailed operating conditions for the laser ablation system and the ICP-MS instrument and data reduction are reported in previous studies (Liu et al., 2008; Huang et al., 2013, 2015). Helium was applied as a carrier gas; and argon was used as the make-up gas and mixed with the carrier gas via a T-connector before entering the ICP. Each analysis includes a background acquisition of approximately 20 s (gas blank) followed by 40 s of data acquisition from the sample. Analytical spots (60 μm) were ablated by 160 successive laser pulses (4 Hz). Element contents were calibrated against multiple-reference materials (GSE-1G, BCR-2G, BIR-1G, BHVO-2G and NIST610) using ^{57}Fe as an internal standard (Gao et al., 2013). Every 8 sample analyses were followed by one analysis of GSE-1G as a quality control to correct the time dependent drift of sensitivity and mass discrimination. Off-line selection and integration of background and analyte signals, and time-drift correction and quantitative calibration were performed by ICPMSDataCal (Liu et al., 2008).

4.2. Iron isotopes

Iron isotopes analyses were performed at the ALS (Analytical Chemistry Laboratory Services) at Scandinavia, Sweden. Minerals separates were extracted from crushed and washed sample fragments, and were selected by handpicking under a binocular microscope to achieve purity >99%. Appropriately 50 mg of powdered magnetite and pyrite separates were dissolved in a 2 ml mixture of ultrapure HCl-HF-HNO_3 using closed-cup 5 ml Teflon vials (Savillex, USA) on a hot plate for 24 h, after which the solution was evaporated dry. The remaining precipitate was taken up in 2 ml of 9 M HCl, and the sample was dried down. The remaining salt was re-dissolved in 0.5 ml of 9 M HCl, at which point it was ready for purification. All samples were purified via anion exchange chromatography in a HCl medium using 2 ml of AG MP-1 M, 100–200 mesh resin loaded in LDPE columns. Fe isotope was analyzed in high mass resolution mode on a Neptune MC-ICP-MS, using the methods outlined by Malinovsky et al. (2003). A Ni spike of the same concentration as Fe was added to each purified sample prior to analysis. Samples

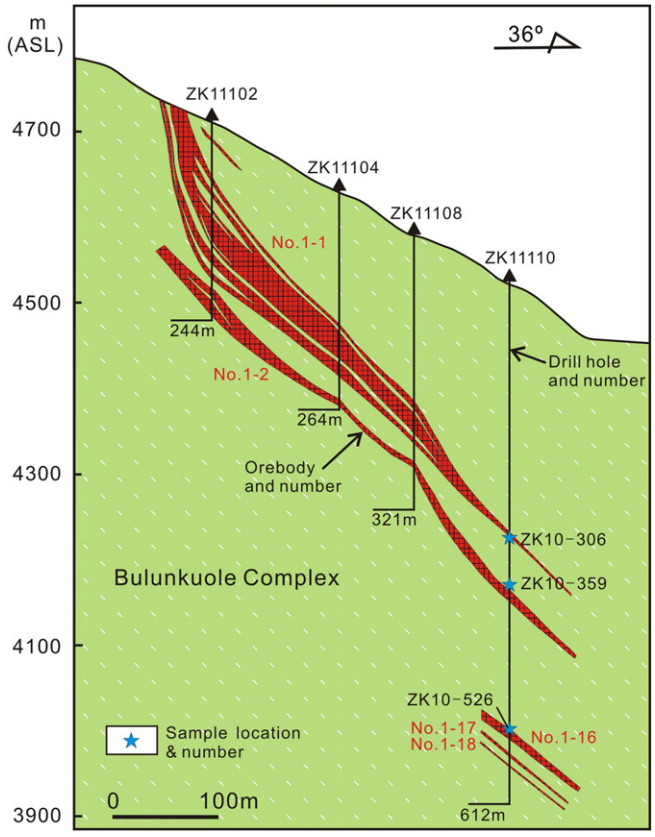

Fig. 3. Geological section of No. 111 prospecting line at the Zankan iron deposit.

were introduced to the instrument in a 0.14 M HNO_3 solution using tandem quartz spray chamber arrangement (cyclone + Scott double pass) and microconcentric PFA nebulizer with Fe concentrations at ca. 2 μg ml^{-1}. All sample and standards were analyzed in duplicate. Fe isotope data are reported using the standard delta notation (in ‰) relative to the reference material IRMM-14:

$$\delta^{56}Fe_{sample}(‰) = \left[\left(^{56}Fe/^{54}Fe\right)_{sample}/\left(^{56}Fe/^{54}Fe\right)_{IRMM-14} - 1\right] \times 1000$$

$$\delta^{57}Fe_{sample}(‰) = \left[\left(^{57}Fe/^{54}Fe\right)_{sample}/\left(^{57}Fe/^{54}Fe\right)_{IRMM-14} - 1\right] \times 1000$$

The internal analytical precision on the measured ratios was better than ±0.005% (at 2σ level). The external reproducibility of the isotopic measurements for standard solutions is better than ±0.1% (2σ) and ±0.2% (2σ) for $\delta^{56}Fe$ and $\delta^{57}Fe$, respectively.

5. Results

5.1. Magnetite trace elements

Most elements in the multicomponent spinel system (Nadoll et al., 2012) are detected. In general, magnetite grains from the Zankan Fe deposit have concentrations of Mg, Al, Ti, V, Mn, Co, Ni, Zn, Ga, and Sn, all above the detection limits, whereas Cr with few spots are below the detection limits. The magnetite grains do not contain Cu, with values generally near or below the detection limits. Trace elements such as Sc, Ge, Rb, Sr, Y, Zr, Nb, Mo, Ag, Cd, In, Ba, Hf, Ta, W, Pb, Bi, Th and U are also measured, but are generally around or below 1 ppm. The average concentrations and standard deviation of selected elements Mg, Al, Ti, V, Cr, Mn, Co, Ni, Zn, Ga, Mo, Sn, and Pb of magnetite from the Zankan deposit, are listed in Table 1, and the detailed analytical results are given in the e-Appendix 1. The minimum concentrations of elements (e.g., Cr and Mo) are below the detection limits. Therefore, the average values of these elements were calculated by assigning all the analyses below detection limit to zero. Magnetite grains from the Zankan show variable contents of Mg (182–1167 ppm), Al (198–2691 ppm), Ti (898–1677 ppm), Mn (821–4695 ppm), Co (7–26 ppm), Ni (1–29 ppm), Zn (5–45 ppm), and Ga (20–62 ppm). The disseminated magnetite grains from sample ZK10-371 show distinctive low V content (234 ppm in average) and high Cr content (53.55 ppm in average). According to Dare et al. (2012), trace elements in magnetite can be lithophile elements (Mg, Al, Cr, Ga, Mn, Nb, Ta, Ti, V, Zr and Hf) and chalcophile elements (Co, Mo, Ni, Pb, Sn and Zn). All magnetite grains have similar continental crust normalized lithophile and chalcophile element patterns (Fig. 6), indicating that they may share a common source. As shown in Fig. 7, Ni shows slight positive correlation with Co (Fig. 7A); Ti positively correlates with Mg and Al (Fig. 7 B and C); and Al negatively correlates with Ga (Fig. 7 D).

5.2. Fe isotopic composition

The Fe isotope compositions of both magnetite and pyrite of the Zankan deposit are listed in Table 2. The magnetite exhibits large variations in Fe isotope composition ($\delta^{56}Fe = -0.3$–$0.5‰$, average 0.2‰; $\delta^{57}Fe = -0.4$–$0.7‰$, average 0.3‰). The pyrite has $\delta^{56}Fe$ and $\delta^{57}Fe$ values of 0.6–0.8‰ (av. 0.7‰) and 0.8–1.2‰ (av. 1.0‰), respectively. Therefore, pyrite has higher Fe-isotope ratios than magnetite. The Fe isotope values for magnetite also increase in ascending stratigraphic sequence as shown by the ZK1110 drill (Fig. 3; Table 2).

6. Discussion

6.1. Magnetite composition and ore-forming conditions

The magnetite is closely associated with hydrothermal minerals such as quartz, anhydrite, pyrite, pyrrhotite and chalcopyrite (Fig. 5B, C, E, F), probably implying that magnetite in the Zankan ores formed from hydrothermal fluids. Furthermore, magnetite from Zankan is enriched in Mn, similar to hydrothermal magnetite from the Coeur d'Alene district (Nadoll et al., 2012). As for hydrothermal magnetite, it is possibly controlled by: fluid composition, temperature, pressure, oxygen fugacity, compositions of hosting rocks or coexisting minerals (Carew, 2004; Nadoll et al., 2014). In this section, we explore possible controlling factors for compositions of magnetite formed by different processes in the Zankan iron deposit.

The fO_2 may control the V content in magnetite. Vanadium can present as V^{3+}, V^{4+} and V^{5+} in natural fluids, but only V^{3+} can be highly partitioned into magnetite. It is clear that V can be enriched in magnetite formed from reducing fluids (Toplis and Carroll, 1995; Banlan et al., 2006; Bordage et al., 2011; Nadoll et al., 2014). Titanium has only one valence state in hydrothermal fluids and thus has a roughly constant partition coefficient between magnetite and fluids (Chung et al., 2015). Magnetite formed by reducing fluids has lower Ti/V ratios relative to those in oxidizing fluids. Magnetite grains from samples ZKA1-2, ZK10-531 and ZKA3-1 have high V contents (3466–8468 ppm) (e-Appendix 1) and low Ti/V ratios (0.11–0.27), indicating a reduced depositional environment. Magnetite of sample ZK10-371 has low V content and high Ti/V ratios of 3.31–9.76, suggesting a relatively oxidizing condition.

Temperature may have influence on concentrations of some elements in magnetite (Ilton and Eugster, 1989). The incorporations of Ti, Mg and Al in magnetite are largely temperature controlled, preferably linked with high temperature such as in a magmatic system, but they are immobile in low-temperature hydrothermal fluids (Van Baalen, 1993; Nielsen et al., 1994; Toplis and Carroll, 1995; Verlaguet et al.,

Fig. 4. Photographs of ores from the Zankan Fe deposit. (A) Massive ore containing magnetite and pyrite; (B), (C) Massive ore containing magnetite and laminated pyrite; (D) Banded Fe ore containing magnetite, and quartz; (E) Banded ore containing magnetite, laminated pyrite and anhydrite; (F) Disseminated ore containing magnetite and pyrite. Abbreviations: Mag, magnetite; Py, pyrite; Qz, quartz; Anh, anhydrite.

2006). In the (Al + Mn) vs. (Ti + V) diagram that was suggested to be a good discriminant of formation temperatures of magnetite (Nadoll et al., 2014), all the samples from the Zankan deposit plot in the field of 300–500 °C (Fig. 8). This suggests that the magnetite has possibly precipitated from hot fluids enriched in Al and Ti. The presence of Ti, Al, V and Mg in seawater are commonly associated with volcanic rocks (Carew, 2004; Bhattacharya et al., 2007). Thus, the high Al and Ti contents in the magnetite from the Zankan deposit can be related to hydrothermal fluids derived from submarine magmatism. The magnetite grains from sample ZKA1-2 have relatively high Al + Mn and Ti + V contents compared to the other samples (Fig. 8), which is also supported by the fact that this sample associates with volcanic rocks.

Coexisting mineral phases might also affect compositions of some specific trace elements of the magnetite (Nadoll et al., 2014). In general, silicates are preferably incorporating lithophile elements, whereas chalcophile elements have a strong preference to partition into sulfides (Cygan and Candela, 1995; Frost, 1991; Toplis and Corgne, 2002; Simon et al., 2008). The iron ores from Zankan are composed mainly of magnetite with minor and variable amounts of silicates (e.g., quartz, plagioclase, hornblende, biotite and muscovite) with or without sulfides (e.g., pyrite, pyrrhotite and chalcopyrite) (Figs. 4 and 5). Because V, Cr and Ti are not easily incorporated in the quartz and feldspar compared to magnetite in the iron ores (Neilson, 2003; Nadoll et al., 2014), these silicates rarely affected their concentrations in magnetite. As Co would be highly partitioned into pyrite and chalcopyrite, the magnetite coexisting with sulfides (samples ZK10-371 and ZK10-531) has relatively low concentrations of Co (7.8–13 ppm) compared to the magnetite without coexisting sulfides (samples ZKA1-2 and ZKA3-1; Co = 22–26 ppm). This shows that coexisting sulfides have played a role for trace element concentration in magnetite.

6.2. Pyrite-magnetite Fe isotope fractionation and ore-forming temperature

The pyrite and magnetite from samples (ZKA3-1, ZKPM6-2, ZK10-359, ZK10-539) at Zankan show heavy Fe isotope enrichment relative to IRMM-014, and Fe isotope compositions of pyrite are systematically heavier than those of corresponding magnetite from the some samples. Base on theoretical computation (Polyakov et al., 2007), the relative order of $\delta^{57}Fe$ enrichment is $\delta^{57}Fe_{pyrite} > \delta^{57}Fe_{magnetite}$, probably suggesting Fe isotope equilibrium between the coexisting magnetite and pyrite in the iron ores. The degree of fractionation between phases is a function of temperature. Based on Mössbauer- and INRXS-derived, and DFT calculation data, Polyakov and Mineev (2000), Polyakov et al. (2007) and Blanchard et al. (2009) obtained the reduced Fe

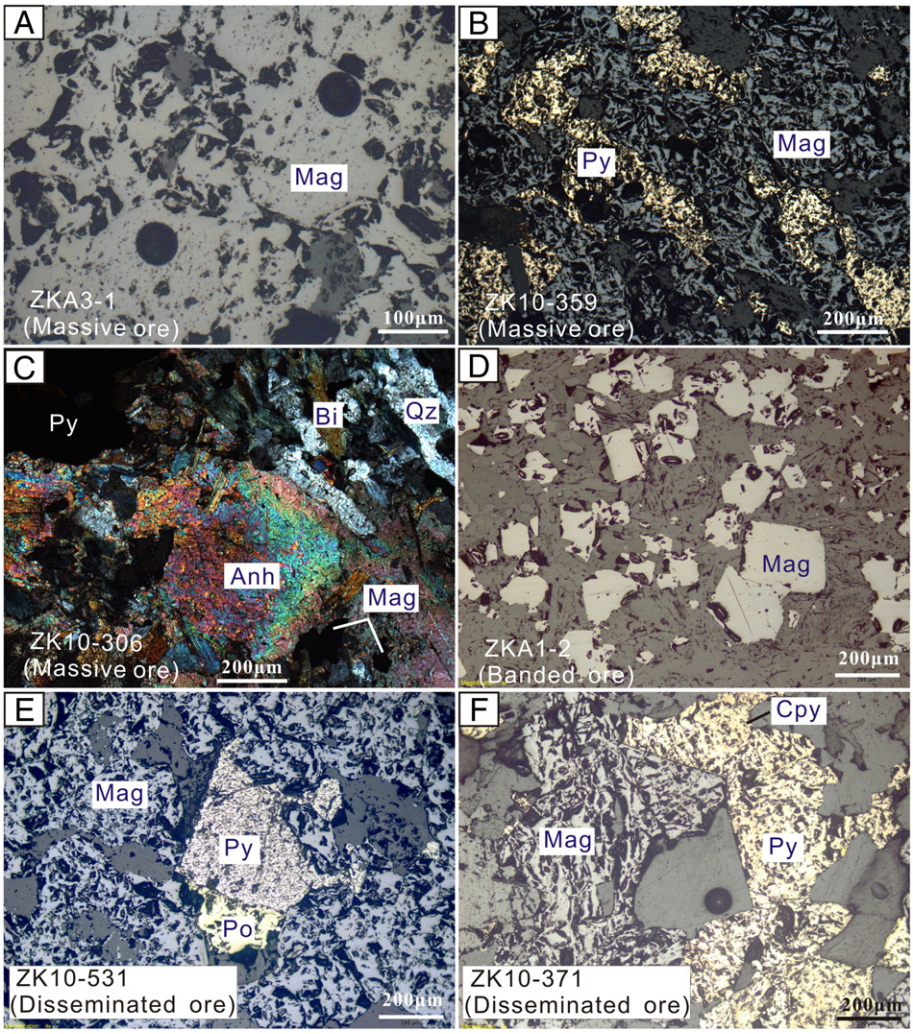

Fig. 5. Photomicrographs of ore minerals in the Zankan iron deposit. (A) Subhedral to anhedral magnetite grains (reflected-light); (B) Anhedral magnetite coexisting with continuous to discontinuous banded pyrite (reflected-light); (C) Anhedral magnetite coexisting with pyrite and anhydrite (cross-polarizing light); (D) Euhedral to subhedral magnetite (reflected-light); (E) Anhedral magnetite coexisting with subhedral pyrite and pyrrhotite (reflected-light); (F) Anhedral magnetite coexisting with pyrite replaced by chalcopyrite (reflected-light). Abbreviations: Mag, magnetite; Py, pyrite; Cpy, chalcopyrite; Po, pyrrhotite; Qz, quartz; Anh, anhydrite; Bi, biotite.

isotope partition function ratios (β-factors) and their variations with temperature for a variety of minerals (including pyrite and magnetite). They concluded that the iron β-factors of pyrite are considerably higher than those of magnetite. However, the Fe isotope fractionation factors between pyrite and magnetite has not been determined yet. To find the pyrite-magnetite Fe isotope fractionation factors ($\Delta\delta Fe_{py\text{-}mag}$), the following equation and available experimental data can be used: the iron $^{57}\beta$-factors of pyrite and magnetite are calculated using the equation (Polyakov and Mineev, 2000; Polyakov et al., 2007):

$$10^3 \ln {}^{57}\beta = A_1 x + A_2 x^2 + A_3 x^3 \quad (1)$$

where $\ln {}^{57}\beta$ relates to $^{57/54}$Fe isotope ratio; T is absolute temperature; A is polynomial coefficient; $A_1 = 1.2437$, $A_2 = -4.8242/10^3$, and $A_3 = 2.6833/10^5$ for pyrite (Blanchard et al., 2009); and $A_1 = 0.95706$,

Table 1
Trace elements (in ppm) of magnetite from the Zankan iron deposit.

Sample no.		Mg	Al	Ti	V	Cr	Mn	Co	Ni	Zn	Ga	Mo	Sn	Pb
D.L.		1.19	1.04	1.53	0.183	1.53	1.14	0.060	0.886	0.637	0.100	0.028	0.299	0.019
ZKA3-1	AVE (n = 6)	1072	1194	1582	6994	5.01	852	25.6	24.6	5.8	59.5	0.098	0.972	0.207
	SD	78.2	19.4	84.0	58.4	3.07	21.0	0.551	2.80	0.594	2.01	0.072	0.230	0.124
ZKA1-2	AVE (n = 12)	717	1193	1245	8269	1.25	4365	23.7	22.6	36.9	41.1	0.097	1.14	0.423
	SD	146	174	195	266	1.83	196	1.52	2.64	2.50	1.95	0.140	0.178	0.896
ZK10-371	AVE (n = 3)	281	2295	1221	234	53.5	2192	7.34	1.57	10.5	21.5	0.347	11.2	0.274
	SD	95.5	565	187	117	45.2	174	0.562	0.339	1.43	1.41	0.196	1.52	0.147
ZK10-531	AVE (n = 3)	428	247	947	3490	2.18	2400	10.6	27.7	43.3	55.0	0.153	12.9	0.273
	SD	304	47.2	9.05	27.6	2.46	167	1.80	1.11	1.19	1.56	0.120	0.584	0.140

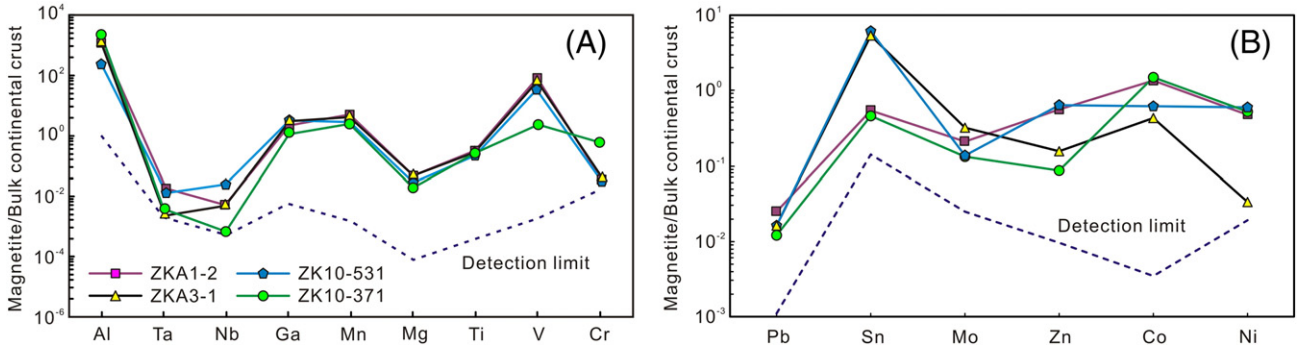

Fig. 6. Bulk continental crust normalized lithophile (A) and chalcophile (B) element patterns of magnetite from the Zankan iron deposit. Trace element contents of bulk continental crust are from Rudnick and Gao (2003).

$A_2 = -4.7296/10^3$, and $A_3 = 4.0703/10^6$ for magnetite (Seto et al., 2003); $x = 10^6/T^2$.

Combined Eq. (1), the temperature dependence of the equilibrium iron isotope fractionation between pyrite and magnetite is given by Eq. (2):

$$\begin{aligned}\Delta\delta^{57}Fe_{py-mag} &= 10^3 ln^{57}\beta_{py} - 10^3 ln^{57}\beta_{mag} \\ &= 1.2437x - 4.8242\times10^{-3}x^2 + 2.6833\times10^{-5}x^3 \\ &\quad -\left(0.95706x - 4.7296\times10^{-3}x^2 + 4.0703\times10^{-6}x^3\right) \\ &= 0.28664x - 0.0946\times10^{-3}x^2 + 2.27627\times10^{-5}x^3\end{aligned} \quad (2)$$

The calculated $\Delta\delta^{57}Fe_{py\text{-}mag}$ values at different temperatures are presented in Fig. 9. In Zankan iron deposit, the pyrite-magnetite pair for samples ZKA3-1 M, ZKPM6-2, ZK10-359 and ZK10-539 show $\Delta\delta^{57}Fe_{py\text{-}mag} = 0.2–1.1‰$ (Table 2). Based on Eq. (2), the calculated temperature is higher than or equal to 236 °C (Fig. 9).

The calculated temperatures may not be very precise. Nevertheless, they show that the ores were formed by high-temperature hydrothermal processes. This is consistent with the conclusion drawn from trace elements of magnetite, i.e., 300–500 °C (Fig. 8).

6.3. Magnetite Fe isotope signature and Fe source

Magnetite for Zankan ores yielded positive and weak negative $\delta^{56}Fe$ (−0.3 to 0.5‰), and are similar to Phanerozoic Fe-rich hydrothermal cherts (Rouxel et al., 2003). Rouxel et al. (2003) interpreted both positive and negative $\delta^{56}Fe$ in Phanerozoic Fe-rich hydrothermal cherts to be the result of partial oxidation during the submarine circulation of low-temperature hydrothermal fluids through volcanic rocks. Hydrothermal vent fluids release Fe with light isotopic composition relative to IRMM-014, ranging from −0.7 to −0.1‰ (Sharma et al., 2001; Beard et al., 2003a; Severmann et al., 2004; Rouxel et al., 2008; Bennett et al., 2009). The most likely reason for the heavy Fe isotope enrichment in Zankan is partial oxidation of $Fe(II)_{aq}$ in the water column. Experiment shows that magnetite is enriched in heavy Fe isotopes by ca. 1.2–1.3‰ in abiotic oxidation processes relative to initial $Fe(II)_{aq}$ at 22 °C (Johnson et al., 2003, 2005). Hence, the heavy Fe isotopic composition of magnetite from Zankan ($\delta^{56}Fe = 0.5‰$ for sample ZK10-526) is

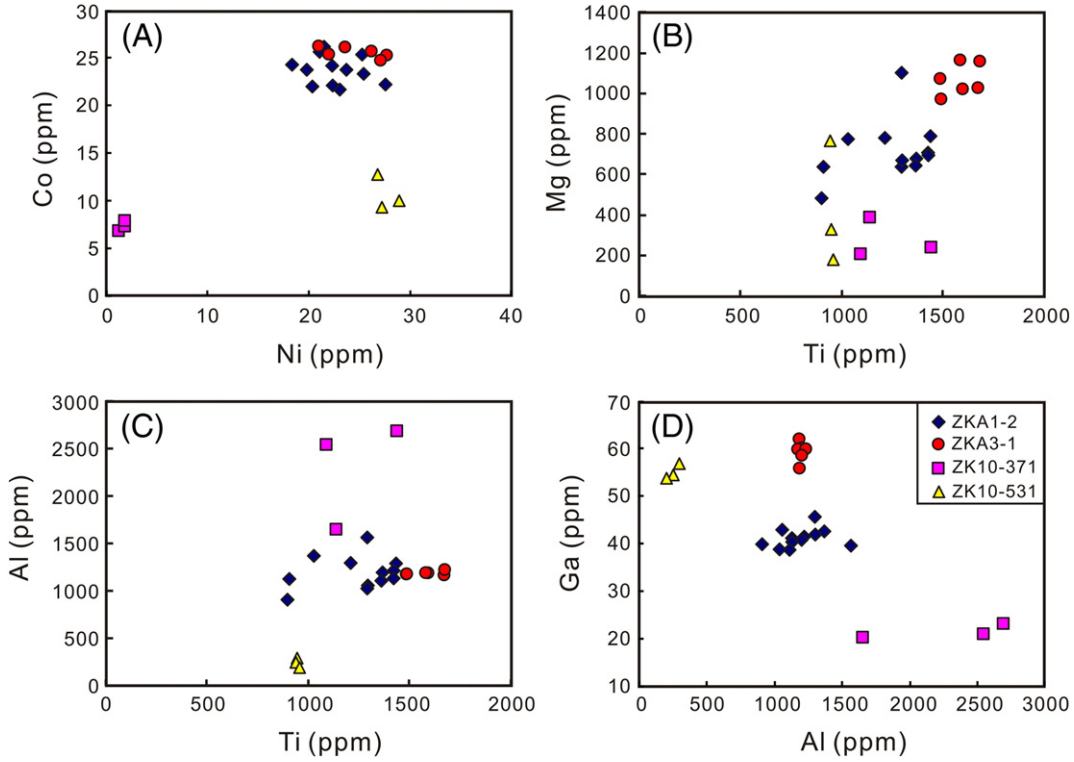

Fig. 7. Bi-plots of Ni vs. Co, Ti vs. Mg, Ti vs. Al, and Al vs. Ga in magnetite from the Zankan iron deposit.

Table 2
Fe isotope compositions of magnetite and pyrite from the Zankan iron deposit.

No.	Sample description	Sample no.	Mineral	$\delta^{56}Fe$	2SD	$\delta^{57}Fe$	2SD	Mineral	$\delta^{56}Fe$	2SD	$\delta^{57}Fe$	2SD	$\Delta\delta^{57}Fe_{py\text{-}mag}$	Temperature (°C)
1	Magnetite iron ore	ZKA3-1M	Magnetite	0.4	0.0	0.6	0.0	Pyrite	0.6	0.0	0.8	0.0	0.2	1100
2	Magnetite iron ore	ZKPM6-2	Magnetite	0.4	0.0	0.6	0.1	Pyrite	0.6	0.0	0.9	0.1	0.3	670
3	Magnetite iron ore	ZK10-359	Magnetite	0.0	0.1	0.0	0.1	Pyrite	0.8	0.0	1.1	0.1	1.1	326
4	Magnetite iron ore	ZK10-526	Magnetite	0.5	0.0	0.7	0.1	Pyrite	0.8	0.1	1.2	0.1	0.5	480
5	Magnetite iron ore	ZK10-306	Magnetite	−0.3	0.0	−0.4	0.0							

best explained by the partial oxidation ($\Delta\delta^{56}Fe_{mag\text{-}Fe(II)aq} = 1.2–1.3‰$) of a seafloor hydrothermal system with $\delta^{56}Fe$ values around −0.7‰. In addition, the $\delta^{56}Fe$ value of magnetite from sample ZK10–359 is near zero, which can be expected if the Fe reservoir had the same isotopic composition as igneous rocks or modern detrital sediments, loess, and aerosols (Beard et al., 2003a, 2003b). The increase of dissolved oxygen in seawater results in quantitative to semiquantitative oxidation of the iron dissolved in the ocean (Mendes et al., 2016). This near-zero $\delta^{56}Fe$ value indicates that magnetite has inherited Fe isotope compositions from ferric oxide/hydroxide precursors in seawater through near-complete oxidation of $Fe(II)_{aq}$ (Johnson et al., 2008). Magnetite for sample ZK10-306 has negative $\delta^{56}Fe$ value (−0.3‰), however, possibly results from microbial activity (Johnson et al., 2005).

The ~0.8‰ variation of $\delta^{56}Fe$ values in magnetite from Zankan deposit is different from Fe oxides of Precambrian sedimentary iron formations, which usually show large variations in $\delta^{56}Fe$ values (Fig. 10A; Johnson et al., 2003, 2008; Dauphas et al., 2004, 2007; Rouxel et al., 2005; Whitehouse and Fedo, 2007; Steinhoefel et al., 2010; Craddock and Dauphas, 2011; Li et al., 2013; Hou et al., 2014). This signature rules out the possibility that the Zankan deposit is a Archean to Paleoproterozoic banded iron farmation, comparable to Algoma-type BIF, as suggested by Dong et al. (2011, 2012).

6.4. Pyrite Fe isotopic signature

Pyrite formation is likely caused by the following events: reactive Fe^{2+} combines with thiosulfate or polysulfide compounds (Schoonen and Barnes, 1991) or with H_2S (Rickard, 1997) to form an aqueous FeS species, which subsequently turns to FeS (mackinawite), the precursor of pyrite (Rickard and Luther, 1997; Benning et al., 2000). Theoretical calculations predict that pyrite (FeS_2) is an isotopically heavy phase relative to $Fe(II)_{aq}$ (Polyakov et al., 2007). By contrast, experiments indicate precipitation of mackinawite (FeS) incorporates lighter isotopes, recording a kinetic fractionation ($\Delta\delta^{56}Fe_{FeS\text{-}Fe(II)aq}$) varying from −0.3 to −0.9‰ during 0–168 h (Butler et al., 2005). However, the Fe isotope exchange and a progressive change towards isotopically heavy FeS on a short (hourly) time scale can push the particulate sulfides heavy (Butler et al., 2005). Thus a rapid isotopic exchange and a slow precipitation are expected to keep a positive fractionation ($\Delta\delta^{56}Fe_{FeS\text{-}Fe(II)aq}$) during pyrite formation in anoxic aquatic systems (Planaavsky et al., 2012). The Proto-Tethys in WKO was a small ocean basin (e.g., Jiang et al., 1992; Pan et al., 2001; Xiao et al., 2005b; Liao et al., 2010). A sedimentation rate for the small seas has been estimated 100 m/myr (Sadler, 1981), suggesting that the 167-m thickness between samples ZK10-359 and ZK10-526 in drill ZK11110 (Fig. 3) reflects 1.67 million years of sedimentation. Both pyrite samples ZK10-359 and ZK10-526 show positive $\delta^{56}Fe$ values (Table 2), which resulted from slow transformation from FeS to pyrite. This understanding is consistent with the results obtained from previous studies equilibrium pyrite precipitation (Polyakov, 1997; Polyakov and Mineev, 2000; Polyakov et al., 2007).

In the Earth history, drastic increase of the atmospheric oxygen abundance occurred at ca. 2.3 Ga and 0.6 Ga (Kasting, 1993, 2001; Chen and Zhao, 1997; Holland, 2002; Canfield, 2005; Rouxel et al., 2005; Guo et al., 2009; Tang and Chen, 2013; Lyons et al., 2014; Chen and Tang, 2016). The sedimentary pyrites formed before the 2.3-Ga Great Oxidation Event display more variable $\delta^{56}Fe$ values of −4.18 to 2.95‰ (Fig. 10B; Rouxel et al., 2005; Archer and Vance, 2006; Nishizawa et al., 2010; Yoshiya et al., 2012), whereas the pyrites formed after 2300 Ma show positive $\delta^{56}Fe$ values of 0.24–1.22‰ (Fig. 10B; Rouxel et al., 2005; Fabre et al., 2011). This difference is interpreted to result from the rise of the atmospheric oxygen, implying for the Great Oxidation Event (Fabre et al., 2011; Yoshiya et al., 2012). The pyrite

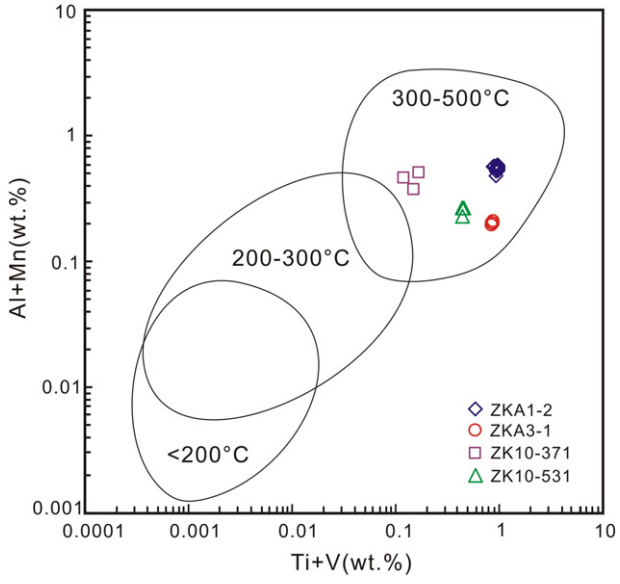

Fig. 8. Plot of Al + Mn vs. Ti + V for different formation temperatures of magnetite. Reference fields are adapted from Nadoll et al. (2014).

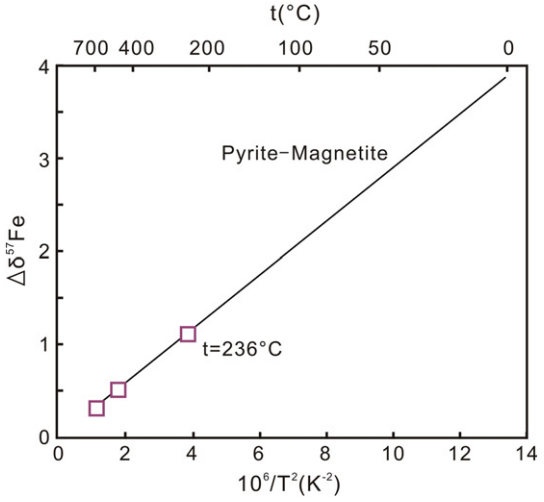

Fig. 9. $\Delta\delta^{57}Fe_{pyrite\text{-}magetite}$ values for Zankan iron deposit minerals and theoretical equilibrium fraction factors as a function of temperature. The black solid line shows fractionation factors for pyrite relative to magnetite. The red squares represent the $\Delta\delta^{57}Fe_{pyrite\text{-}magetite}$ values for samples ZKPM6-2, ZK10-359, ZK10-539 from Zankan deposit. The calculated temperature is ≥236 °C.

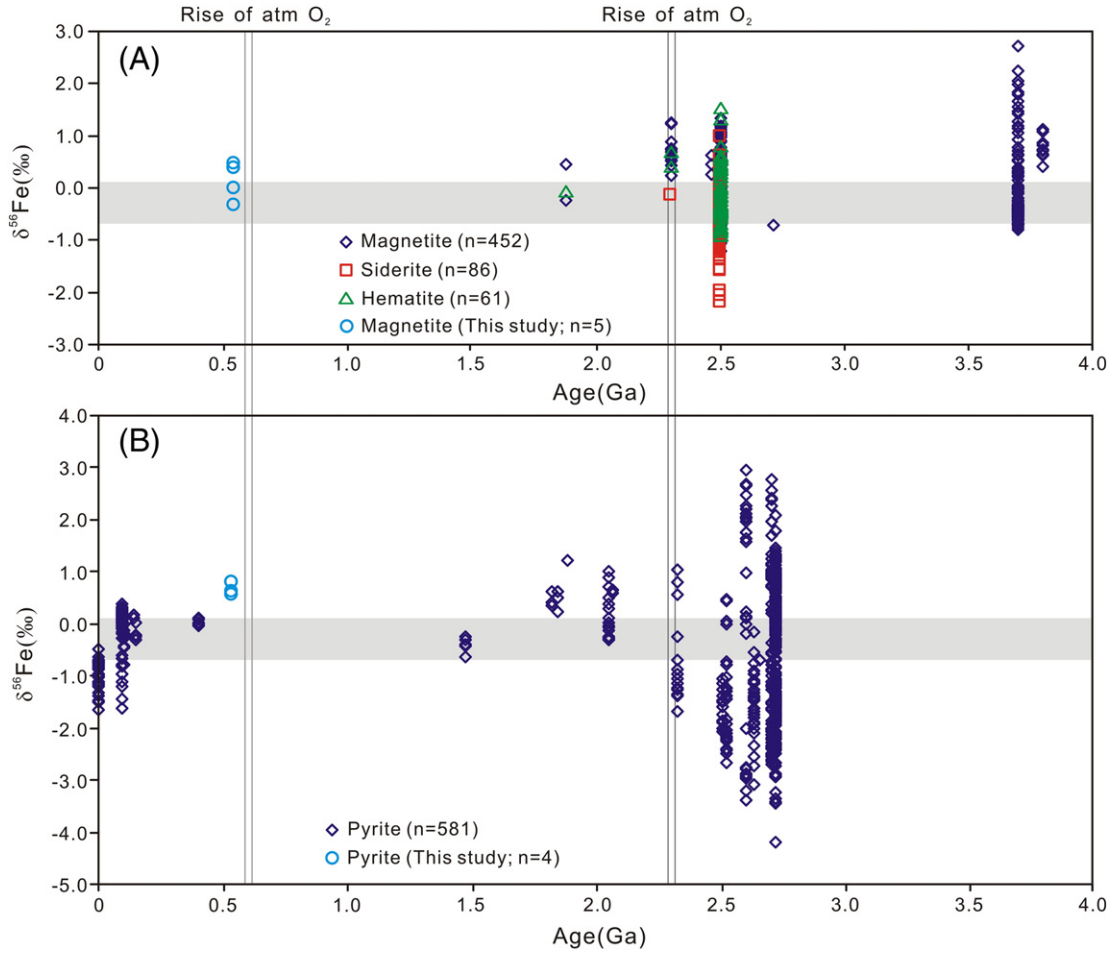

Fig. 10. Temporal evolution of δ^{56}Fe values: (A) δ^{56}Fe values for magnetite from this study (blue circle), and δ^{56}Fe values for magnetite (blue diamond), siderite (red squares), and hematite (green triangle) from sedimentary iron formation from literature (Johnson et al., 2003, 2008; Dauphas et al., 2004, 2007; Rouxel et al., 2005; Whitehouse and Fedo, 2007; Steinhoefel et al., 2010; Craddock and Dauphas, 2011; Li et al., 2013; Hou et al., 2014); (B) δ^{56}Fe values for pyrite from this study (blue circle) and δ^{56}Fe values for sedimentary pyrite (blue diamond) from literature (Matthews et al., 2004; Rouxel et al., 2005; Archer and Vance, 2006; Severmann et al., 2006; Clayton et al., 2007; Jenkyns et al., 2007; Fehr et al., 2008, 2010; Nishizawa et al., 2010; Fabre et al., 2011; Yoshiya et al., 2012). The gray area corresponds to δ^{56}Fe values of Fe derive from igneous rocks (at 0.1%) and hydrothermal vent fluids (−0.69 to −0.12‰) (Sharma et al., 2001; Beard et al., 2003a; Severmann et al., 2004; Rouxel et al., 2008; Bennett et al., 2009).

δ^{56}Fe values of the Zankan deposit range 0.6–0.8‰, which appear to be the characteristic of the time after atmospheric oxygen rise (Fig. 10B). This interpretation is fairly consistent with the Phanerozoic pyrite δ^{56}Fe trend, as exemplified by the Devonian, Jurassic and Cretaceous sedimentary pyrites which have δ^{56}Fe values of −0.04 to 0.12‰, −0.31 to 0.01‰, and −0.77 to 0.16‰, respectively (Fig. 10B; Matthews et al., 2004; Rouxel et al., 2005; Clayton et al., 2007).

6.5. Is Zankan an Algoma-type BIF?

The Zankan deposit was considered to be an Algoma-type banded iron formation (Dong et al., 2011, 2012; Feng et al., 2011), which is definitely worthy of further discussion. According to Gross (1980, 1995), the Algoma-type banded iron formations (BIFs) are typically Archean magnetite-quartz-silicate assemblages hosted in volcanic rocks, greywackes, turbidites and fine-grained clastic sediments, formed in volcanic arcs or back-arc basins, spreading ridges and rifts (Gross, 1995). They are characterized by alternating magnetite and quartz laminations or bandings formed by seafloor hydrothermal processes near volcanic center under a condition with pH range of from 1.25 to 5.5 (Zhu et al., 2014). Classic Algoma-type Fe deposits are exemplified by the Archean BIFs in Yilgarn and Pilbara blocks, Australia (Angerer et al., 2012; Teitler et al., 2014), Carajás deposits in Brazil (Figueired e Silva et al., 2008; Fabre et al., 2011), Gongchangling deposit in NE China (Sun et al., 2014), and the Algoma deposit itself in Canada (Gross, 1980, 1995).

The Zankan Fe deposit shows some similarities with the Algoma-type BIFs, including a volcanic-sedimentary host succession, lamination and banding textures. Magnetite is the ore mineral, associated with gangue minerals such as quartz and actinolite or pyroxene (Li et al., 2014). However, the Zankan deposit shows a unique mineral association of magnetite, pyrite and anhydrite with variable ratios. Precambrian BIFs are temporally associated with organic matter-rich black shales (e.g., Simonson, 2003), commonly either overlain or underlain by organic matter-rich and sulfidic shales and, in some case, are interstratified with them (Bekker et al., 2010). By contrast, in Zankan Fe deposit, organic matter-rich and sulfidic shales have not been observed yet. Algoma-type BIFs occur in volcanic-sedimentary sequences of greenstone belts aged from Eoarchean to late Paleoproterozoic (Goodwin, 1973; James, 1983; Isley and Abbott, 1999; Huston and Logan, 2004). However, iron mineralization at Zankan occurred at ca. 536 Ma (Lin, 2015; Dong et al., 2016), without any other base metal as by-product. Fe oxides of Algoma-type BIFs are formed by partial oxidation of Fe(II) species in seawater under low atmospheric oxygen level before GOE, and thus their δ^{56}Fe values are widely variable and generally positive (Dauphas et al., 2004, 2007; Whitehouse and Fedo, 2007; Fabre et al., 2011; Planaavsky et al., 2012). The Zankan deposit, however, shows slightly variable magnetite δ^{56}Fe values (Fig. 10). As revealed by in-

situ trace element detection, the magnetite grains from Zhankan have much higher Al + Mn and Ti + V concentrations, and lower Ni/(Cr + Mn) ratios than those from BIFs (Fig. 11; Dupuis and Beaudoin, 2011; Nadoll et al., 2014). The Algoma-type BIFs show high SiO_2 content of 48.9 wt.% in average (Gross and MCleod, 1980), but the SiO_2 contents of the Zankan deposit has are very low, average 21.02 wt.% (Dong et al., 2016).

6.6. A seafloor hydrothermal exhalative system?

Ridler (1971)defined exhalites as chemical sedimentary rocks formed by hydrothermal fluids venting. Based on lithological and geochemical data, exhalites are broadly considered as amorphous Fe ± Mn ± Si ± S ± Ba ± B phases precipitatated from seafloor hydrothermal vents and plumes (Kimberley, 1989; Isley, 1995; Peter, 2003; Grenne and Slack, 2005). Such seafloor hydrothermal exhalites are generally associated with VMS-type Cu-Zn and SEDEX-type Pb-Zn deposits (e.g., Sangster, 1978; Spry et al., 2000; Peter, 2003). Exhalites cover a wide time span, from Archean to Mesozoic (e.g., Bekker et al., 2010; Slack et al., 2009; Peter, 2003). Most exhalites are tabular in form and conformable to bedding within enclosing volcanic or sedimentary strata (Spry et al., 2000; Slack and Shanks, 2012). Significant silica-iron exhalites include the Mount Windsor Subprovince, SE Australia (Davidson et al., 2001), Bathurst Mining Camp, Canada (Peter and Goodfellow, 1996, 2003), Tyrone Igous Complex, Northern Ireland (Hollis et al., 2015), and Pecos greenstone belt (Slack et al., 2009).

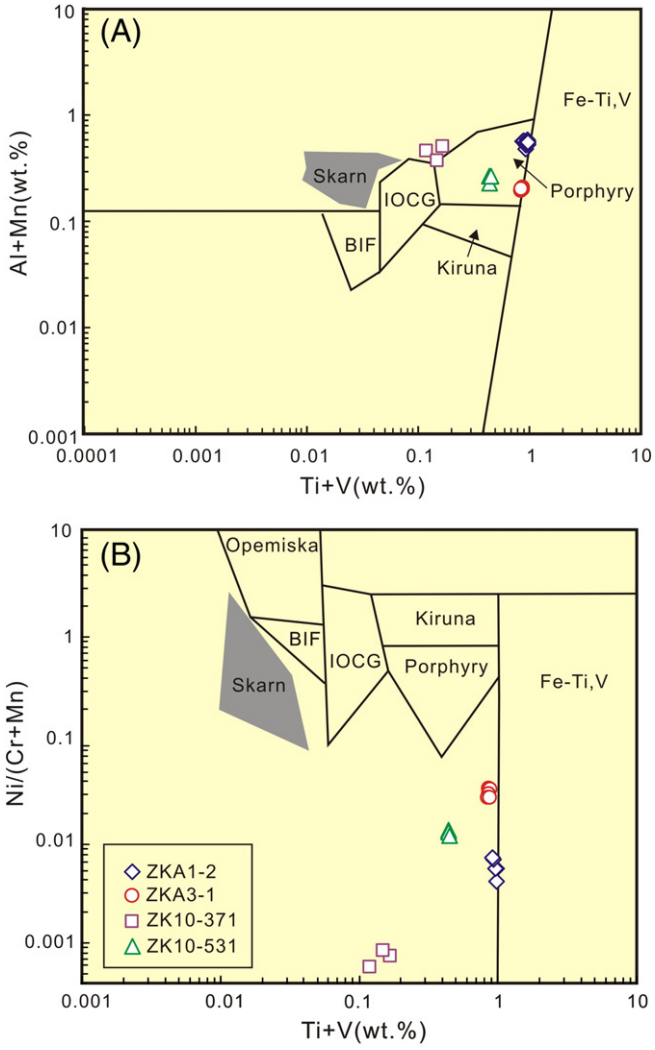

Fig. 11. Plots of Al + Mn vs. Ti + V (A) and Ni (Cr + Mn) vs. Ti + V (B) for LA-ICP-MS data of magnetite from the Zankan iron deposit (base map from Dupuis and Beaudoin, 2011). BIF: banded iron formation; Skarn: Fe–Cu skarn deposits; IOCG: iron oxide-copper-gold deposits; Porphyry: porphyry Cu deposits; Kiruna: Kiruna apatite-magnetite deposits; Fe–Ti, V: magmatic Fe–Ti-oxide deposits.

Iron mineralization at Zankan exhibits most of the characteristics of seafloor hydrothermal exhalites, such as a mineralogical association (magnetite, pyrite and anhydrite), volcanic and sedimentary host rocks, stratiform or near-bedded orebodies, and massive and lamination structures. Compared to exhalites associated with VMS or SEDEX systems (Peter, 2003; Slack and Shanks, 2012), the lithologies at Zankan are richer in iron oxides (e.g., hematite, magnetite), poor in silica and silicates (e.g., greenalite, stilpnomelane, grunerite), carbonates (e.g., dolomite, calcite, siderite, ankerite), with only a trace of chalcopyrite, sphalerite and galena. Sulfides at Zankan mainly include pyrite and pyrrhotite; and sulfates are mainly barite, anhydrite and gypsum). The Al_2O_3 contents in exhalites are generally considered as contribution from terrestrial detrital components (Peter, 2003), which range 0.16–5.19 wt.% at Zankan (Dong et al., 2016), lower than those in Fe-rich lithologies in the world (6–7 wt.% in average; Peter, 2003). This suggests that the Zankan deposit might have formed in a deep sea.

In the discriminations of magnetite from mineral deposits of different genetic types (Dupuis and Beaudoin, 2011), most of magnetite samples from the Zankan deposit plot in the Porphyry field (Fig. 11A). This also suggests that the Zankan deposit was mainly formed by hydrothermal process, instead of magmatic differentiation or normal chemical sedimentation. We suggest the Zankan Fe deposit to be a seafloor hydrothermal system, considering that: (1) the orebodies are stratiform or layered in shape and conformably hosted in a volcanic succession (Fig. 2; Lin, 2015); (2) the ores display sedimentary features (Fig. 4B–E); (3) mineral assemblage is characterized by Fe-oxides, Fe-sulfides, sulfates (barite, anhydrite and gypsum), and minor and variable content of quartz; (4) magnetite shows high contents of Ti, Al, and V, which is generally considered as a marker of relatively reduced seafloor hydrothermal systems (Carew, 2004); (5) the $\Delta\delta^{57}Fe_{py\text{-}mag}$ values range 0.2–1.1‰, indicating a high temperature precipitation environment (≥ 236 °C); and (6) the pyrite $\delta^{34}S$ values range from 3.2 to 32.8‰ (Dong et al., 2016), suggesting a submarine deposition.

6.7. Tectonic setting

Laser ablation-ICPMS (LA-ICPMS) U-Pb dating of zircons from the volcanic rocks shows that the Zankan iron deposit was formed at ca. 536 Ma (Lin, 2015; Dong et al., 2016), when the Proto-Tethys oceanic plate southwardly subducted beneath the SKT and TTT (Liao et al., 2010; Jia et al., 2013; Dong et al., 2016). This subduction caused the Early Paleozoic magmatism and mineralization in the West Kunlun Orogen (Xu et al., 1994; Xiao et al., 2005a; Liao et al., 2010; Yan et al., 2012a, 2012b; Jia et al., 2013; Yang, 2013). To explain the genesis of the Zankan Fe deposit, a metallogenic model is proposed and schematically illustrated in Fig. 12. Intense magmatic activity in a volcanic arc provided abundant ore-forming metals, caused seafloor hydrothermal exhalation which mixed with seawater. Hydrothermal fluids could percolate and extract the metals from submarine volcanic rocks, and then discharge the metals near hydrothermal vents.

7. Concluding remarks

(1) The Zankan deposit is hosted in the pre-Devonian Bulunkuole metamorphic volcanic-sedimentary rocks. The iron orebodies commonly are mostly conformable with their host rocks, and stratiform and near-bedded in shape. The ores show lamination and banding structures, mainly composed of Fe-oxides (magnetite), Fe-sulfides (pyrite and pyrrhotite) and sulfates (barite, anhydrite and gypsum), together with variable contents of quartz.
(2) Magnetite in ores from the Zankan deposit has variable contents of Mg, Al, Ti, V, Mn, Co, Ni, Zn, and Ga, which can be related to a

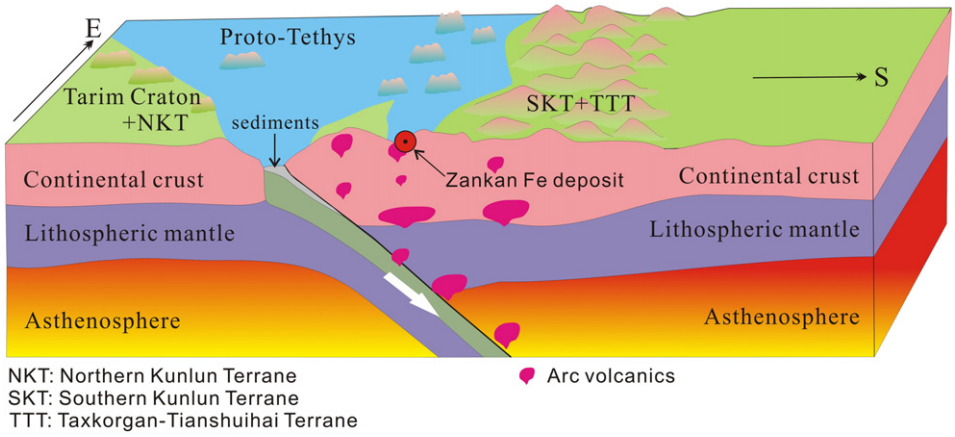

Fig. 12. Tectonic setting for the Zankan iron deposit and host-rocks.

seafloor hydrothermal process. Oxygen fugacity, temperature and co-precipitating mineral phases control the chemical composition of magnetite.

(3) Magnetite has δ^{56}Fe values of −0.3 to 0.5‰, which suggests the partial oxidation of Fe^{2+} to Fe^{3+}. The pyrite δ^{56}Fe values range 0.6–0.8‰, which is interpreted to the result of the atmospheric oxygen rise in Late Neoproterozoic. The Fe isotope fractionation between pyrite and magnetite suggest that the Zankan deposit formed was mainly a high temperature seafloor hydrothermal system.

(4) The Zankan iron deposit was formed in an Early Cambrian volcanic arc related to the southward subduction of Proto-Tethyan plate beneath the South Kunlun and Taxkorgan-Tianshuihai terranes.

Supplementary data to this article can be found online at http://dx.doi.org/10.1016/j.oregeorev.2016.09.020.

Acknowledgments

This work was jointly granted by the National Natural Science Foundation of China (Nos. 41402061, 41672086, U1403292), the China Geological Survey Bureau (1212011140056), and National Key Technology Research and Development Program of the Ministry of Science and Technology of China (2015BAB05B04). We thank Ilia Rodushkin and Dr. Xiaohui Sun helped the laboratory work. Professor Lianhui Dong, Xun Qu, Jihong Li, Changrong Feng and Qiugen Li, Master Yanshuang Wu, as well as the Geological Survey of Xinjiang helped the field investigation. Careful corrections, relevant comments and constructive suggestions from Professor D. Huston and an anonymous reviewer and Professor Franco Pirajno greatly improved our knowledge and the quality of our paper.

References

Angerer, T., Hagemann, S.G., Danyushevsky, L.V., 2012. Geochemical evolution of the banded iron formation-hosted high-grade iron ore system in the Koolyanobbing greenstone belt. West. Aust. Econ. Geol. 107, 599–644.

Archer, C., Vance, D., 2006. Coupled Fe and S isotope evidence for Archean microbial Fe (III) and sulfate reduction. Geology 34, 153–156.

Banlan, E., De Villiers, J.P.R., Eeckhout, S.G., Glatzel, P., Toplis, M.J., Fritsch, E., Allard, T., Galoisy, L., Calas, G., 2006. The oxidation state of vanadium in titanomagnetite from layered basic intrusions. Am. Mineral. 91, 953–956.

Beard, B.L., Johnson, C.M., Skulan, J.L., Nealson, K.H., Cox, L., Sun, H., 2003a. Application of Fe isotopes to tracing the geochemical and biological cycling of Fe. Chem. Geol. 195, 87–117.

Beard, B.L., Johnson, C.M., Von Damm, K.L., Poulson, R.L., 2003b. Iron isotope constraints on Fe cycling and mass balance in oxygenated earth oceans. Geology 31, 629–632.

Beaudoin, G., Dupuis, C., 2009. Iron-oxide trace element fingerprinting of mineral deposit types. In: Corriveau, L., Mumin, A.H. (Eds.), Exploring for Iron Oxide Copper-Gold Deposits: Canada and Global Analogues: GAC Short Course Notes, pp. 107–121.

Bekker, A., Slack, J.F., Planavsky, N., Krapež, B., Hofmann, A., Konhauser, K.O., Rouxel, O.J., 2010. Iron formation: the sedimentary product of a complex interplay among mantle, tectonic, oceanic, and biospheric processes. Econ. Geol. 105, 467–508.

Bennett, S.A., Rouxel, O., Schmidt, K., Garbe-Schönberg, D., Statham, P.J., German, C.R., 2009. Iron isotope fractionation in a buoyant hydrothermal plume, 5°S mid-Atlantic ridge. Geochim. Cosmochim. Acta 73, 5619–5634.

Benning, L.G., Winkin, R.T., Barnes, H.L., 2000. Reaction pathways in the Fe–S system below 100 °C. Chem. Geol. 167, 25–51.

Bhattacharya, H.N., Chakrabortym, I., Ghosh, K.K., 2007. Geochemistry of some banded iron-formations of the Archean Supracrustals, Jharkhand-Orissa region, India. J. Earth Syst. Sci. 116, 245–259.

Blanchard, M., Poitrasson, F., Méheut, M., Lazzeri, M., Mauri, F., Balan, E., 2009. Iron isotope fractionation between pyrite (FeS_2), hematite (Fe_2O_3) and siderite ($FeCO_3$): a first-principle density functional theory study. Geochim. Cosmochim. Acta 73, 6565–6578.

Bordage, A., Baland, E., Villiers, J.R., Cromarty, R., Juhim, A., Carvallo, C., Calas, G., Sunder Raju, P.V., Glatzel, P., 2011. V oxidation state in Fe-Ti oxides by high-energy resolution fluorescence-detected X-ray absorption spectroscopy. Phys. Chem. Miner. 38, 449–458.

Butler, I.B., Archer, C., Vance, D., Oldroyd, A., Rickard, D., 2005. Fe isotope fractionation on FeS formation in ambient aqueous solution. Earth Planet. Sci. Lett. 236, 430–442.

Canfield, D.E., 2005. The early history of atmospheric oxygen. Annu. Rev. Earth Planet. Sci. 33, 1–36.

Carew, M.J., 2004. Controls on Cu-Au Mineralisation and Fe Oxide Metasomatism in the Eastern Fold Belt, NW Queensland, Australia (Unpublished thesis) James Cook University, Queensland.

Chen, C.J., 2012. Study of Metallogenic Regularity and Prospecting Direction of Iron Deposit in Taxkorgan Area, Xinjiang Province Master Thesis China University of Geosciences, Wuhan (90pp.) (in Chinese with English abstract).

Chen, S.Y., 2013. Geological Characteristics of the Magnetite Deposit in Taxkorgan Mining Area, Xinjiang Master Thesis China University of Geosciences, Beijing (44pp.) (in Chinese with English abstract).

Chen, Y.J., Santosh, M., 2014. Triassic tectonics and mineral systems in the Qinling Orogen, central China. Geol. J. 49, 338–358.

Chen, Y.J., Tang, H.S., 2016. The great oxidation event and its records in North China Craton. In: Zhai, M.G., Zhao, Y., Zhao, T.P. (Eds.), Main Tectonic Events and Metallogeny of the North China Craton. Springer, Berlin, pp. 281–303.

Chen, Y.J., Zhao, Y.C., 1997. Geochemical characteristics and evolution of REE in the early Precambrian sediments: evidences from the southern margin of the North China craton. Episodes 20 (2), 109–116.

Chen, Y.J., Santosh, M., Somreville, I.D., Chen, H.Y., 2014. Indosinian tectonics and mineral systems in China: an introduction. Geol. J. 49, 331–337.

Chen, Y., Wu, L., Zhang, C.J., Cui, X.M., Li, Z.C., Niu, J., 2013. Primary study on geological characteristics of Zankan iron deposit in Tashkurgan in Western Kunlun in Xinjiang Uygur Autonomous Region. Land and Resources in Shandong Province. 29, pp. 18–22 in Chinese with English abstract.

Chen, J.K., Yan, C.H., Zhang, W.S., Gao, T.C., Lu, X.H., Zhang, S.B., Hu, X.C., 2011. Geological characteristics and prospecting direction of the magnetite iron deposits in the Taxkorgan, Xinjiang. Geol. Surv. Res. 34, 179–189 (in Chinese with English abstract).

Chen, W.T., Zhou, M.F., Li, X., Gao, J.F., Hou, K., 2015. In-situ LA-ICP-MS trace elemental analyses of magnetite: the Khetri copper belt in Rajasthan province, NW India. Ore Geol. Rev. 65, 929–939.

Chung, D., Zhou, M.F., Gao, J.F., Chen, W.T., 2015. In-situ LA-ICP-MS trace elemental analyses of magnetite: the late Palaeoproterozoic Sokoman Iron Formation in the Labrador Trough, Canada. Ore Geol. Rev. 65, 917–928.

Clayton, R.E., Nederbragt, A.J., Malinovsky, D., Andersson, P., Thurow, J., 2007. Iron isotope geochemistry of mid-cretaceous organic-rich sediments at Demerara Rise (ODP Leg 207). Proc. NZ Ecol. Soc. 207, 1–14.

Craddock, P.R., Dauphas, N., 2011. Iron and carbon isotope evidence for microbial iron respiration throughout the Archean. Earth Planet. Sci. Lett. 303, 121–132.
Cygan, G.L., Candela, P.A., 1995. Preliminary study of gold partitioning among pyrrhotite, pyrite, magnetite, and chalcopyrite in gold-saturated chloride solutions at 600 to 700 °C, 140 MPa, 1400 bars. In: Thompson, J.F.H. (Ed.), Magmas, Fluids, and Ore Deposits. Mineralogical Association of Canada, pp. 129–137 Short Course.
Dare, S.A.S., Barnes, S.J., Beaudoin, G., 2012. Variation in trace element content of magnetite crystallized from a fractionating sulfide liquid, Sudbury, Canada: implications for provenance discrimination. Geochim. Cosmochim. Acta 88, 27–50.
Dauphas, N., Rouxel, O., 2006. Mass spectrometry and natural variations of iron isotopes. Mass Spectrom. Rev. 25, 515–550.
Dauphas, N., van Zuilen, M., Busigny, V., Lepland, A., Wadhwa, M., Janney, P.E., 2007. Iron isotope, major and trace element characterization of early Archean supracrustal rocks from SW Greenland: protolith identification and metamorphic overprint. Geochim. Cosmochim. Acta 71, 4745–4770.
Dauphas, N., van Zuilen, M., Wadhwa, M., Davis, A.M., Marty, B., Janney, P.E., 2004. Clues from Fe isotope variations on the origin of early Archean BIFs from Greenland. Science 306, 2077–2080.
Davidson, G.J., Stolz, A.J., Eggins, S.M., 2001. Geochemical anatomy of silica iron exhalites: evidence for hydrothermal oxyanion cycling in response to vent fluid redox and thermal evolution (Mt. Windsor Subprovince, Australia). Econ. Geol. 96, 1201–1226.
Dong, L.H., Chen, Y.J., Li, J.H., Qu, X. (Eds.), 2016. Precambrian mineralization and exploration targeting in the circum Tarim area. Geological Survey of Xinjiang Uygur Autonomous Region, Urumqi (Research report No. 1212011140056). in Chinese.
Dong, L.H., Feng, J., Zhuang, D.Z., Liu, B., Li, F.M., Qu, X., Jiang, Y.H., Zhou, G., 2011. Xinjiang geological mineral exploration retrospect and prospect. Xinjiang Geol. 29, 1–6 in Chinese with English abstract.
Dong, L.H., Li, J.H., Feng, J., Zhuang, D.Z., Liu, B., Li, F.M., Qu, X., Jiang, Y.H., 2012. The main achievement and progress of Xinjiang geology and mineral exploration in 2011. Xinjiang Geol. 30, 1–4 in Chinese with English abstract.
Dupuis, C., Beaudoin, G., 2011. Discriminant diagrams for iron oxide trace element fingerprinting of mineral deposit types. Mineral. Deposita 46, 1–17.
Fabre, S., Nédélec, A., Poitrasson, F., Strauss, H., Thomazo, C., Nogueira, A., 2011. Iron and Sulphur isotopes from the Carajás mining province (Pará, Brazil): implications for the oxidation of the ocean and the atmosphere across the Archaean-Proterozoic transition. Chem. Geol. 289, 124–139.
Fehr, M.A., Andersson, P.S., Hålenius, U., Gustafsson, Ö., Mörth, C.M., 2010. Iron enrichments and Fe isotopic compositions of surface sediments from the Gotland Deep Baltic Sea. Chem. Geol. 277, 310–322.
Fehr, M.A., Andersson, P.S., Hålenius, U., Mörth, C.M., 2008. Iron isotope variations in Holocene sediments of the Gotland deep Baltic Sea. Geochim. Cosmochim. Acta 72, 807–826.
Feng, C.R., Wu, H.C., Chen, Y., 2011. Geological characteristics and genesis of the Zankan iron deposit in Taxkorgan' Xinjiang. Geotecton. Metallog. 35, 404–409 in Chinese with English abstract.
Figueired e Silva, R.C., Lobato, L.M., Rosière, C.A., 2008. A hydrothermal origin for the jaspilite-hosted giant Sierra Norte deposits in the Cajajas Mineral Province, Para State, Brazil. Rev. Econ. Geol. 15, 255–290.
Frost, B.R., 1991. Magnetic petrology: factors that control the occurrence of magnetite in crustal rocks. In: Lindsley, D.H. (Ed.), Oxide Minerals: Petrologic and Magnetic Significance. Rev. Mineral. Mineral. Soc. Am., pp. 489–509.
Gao, J.F., Zhou, M.F., LightFoot, P.C., Wang, C.Y., Qi, L., Sun, M., 2013. Sulfide saturation and magma emplacement in the formation of the Permian Huangshandong Ni-Cu sulfide deposit, Xinjiang, Northwestern China. Econ. Geol. 108, 1833–1848.
Goodwin, A.M., 1973. Archean iron-formations and tectonic basins of the Canadian Shield. Econ. Geol. 68, 915–933.
Grenne, T., Slack, J.F., 2005. Geochemistry of jasper beds from the Ordovician Løkken ophiolite, Norway—origin of proximal and distal siliceous exhalites. Econ. Geol. 100, 1511–1527.
Gross, G.A., 1980. A classification of iron-formation based on depositional environments. Can. Mineral. 18, 215–222.
Gross, G.A., 1995. Algoma-type iron-formation. In: Eckstrand, O.R., et al. (Eds.), Geology of Canadian Mineral Deposit Types: Geological Survey of Canada. Geology of Canada, pp. 66–73 (No. 8).
Gross, G.A., Mcleod, C.R., 1980. A preliminary assessment of the chemical composition of iron formations in Canada. Can. Mineral. 18, 223–229.
Guo, Q.J., Strauss, H., Kaufman, A.J., Schröder, S., Gutzmer, J., Wing, B., Baker, M.A., Bekker, A., Jin, Q.S., Kim, S.T., Farquhar, J., 2009. Reconstructing Earth's surface oxidation across the Archean-Proterozoic transition. Geology 37, 399–402.
Holland, H.D., 2002. Volcanic gases, black smokers, and the great oxidation event. Geochim. Cosmochim. Acta 66, 3811–3826.
Hollis, S.P., Cooper, M.R., Herrington, R.J., Roberts, S., Earls, G., Verbeeten, A., Piercey, S.J., Archibald, S.M., 2015. Distribution, mineralogy and geochemistry of silica-iron exhalites and related rocks from the Tyrone igneous complex: implications for VMS. J. Geochem. Explor. 159, 148–168.
Hou, K.J., Li, Y.H., Gao, J.F., Liu, F., Qin, Y., 2014. Geochemistry and Si-O-Fe isotope constraints on the origin of banded iron formations of the Yuanjiacun formation, Lvliang Group, Shanxi, China. Ore Geol. Rev. 57, 288–298.
Hu, L., 2014. Geological Characteristics and Prospecting Direction of the Magnetite Deposit in Laobing Mining Area, Xinjiang Master Thesis China University of Geosciences, Beijing (66pp.) (in Chinese with English abstract).
Huang, X.W., Zhou, M.F., Qi, L., Gao, J.F., Wang, Y.W., 2013. Re-Os isotopic ages of pyrite and chemical composition of magnetite from the Cihai magmatic-hydrothermal Fe deposit, NW China. Mineral. Deposita 48, 925–946.
Huang, X.W., Zhou, M.F., Qiu, Y.Z., Qi, L., 2015. In-situ LA-ICP-MS trace elemental analyses of magnetite: the Bayan obo Fe-REE-Nb deposit, North China. Ore Geol. Rev. 65, 884–899.
Huston, D.L., Logan, G.A., 2004. Barite, BIFs and bugs: evidence for the evolution of the Earth's early hydrosphere. Earth Planet. Sci. Lett. 220, 41–55.
Ilton, E.S., Eugster, H.P., 1989. Base metal exchange between magnetite and a chloride-rich hydrothermal fluid. Geochim. Cosmochim. Acta 53, 291–301.
Isley, A.E., 1995. Hydrothermal plumes and the delivery of iron to banded iron formation. J. Geol. 103, 169–185.
Isley, A.E., Abbott, D.H., 1999. Plume-related mafic volcanism and the deposition of banded iron formation. J. Geophys. Res. 104, 15461–15477.
James, H.L., 1983. Distribution of banded iron-formation in space and time. In: Trendall, A.F., Morris, R.C. (Eds.), Iron-formation: Facts and Problems. Elsevier, Amsterdam, pp. 471–490.
Jenkyns, H.C., Matthews, A., Tsikos, H., Erel, Y., 2007. Nitrate reduction, sulfate reduction, and sedimentary iron isotope evolution during the Cenomanian-Turonian oceanic anoxic event. Paleoceanography 22, PA3208. http://dx.doi.org/10.1029/2006PA001355.
Ji, W.H., Li, R.S., Chen, C.J., He, S.P., Zhao, Z.M., Bian, X.W., Zhu, H.P., Cui, J.G., Ren, J.G., 2011. The discovery of Palaeoproterozoic volcanic rocks in the Bulunkuoler Group from the Tianshuihai Massif in Xinjiang of Northwest China and its geological significance. Sci. China Earth Sci. 54, 61–72.
Jia, R.Y., Jiang, Y.H., Liu, Z., Zhao, P., Zhou, Q., 2013. Petrogenesis and tectonic implications of early Silurian high-K calc-alkaline granites and their potassic microgranular enclaves, western Kunlun orogen, NW Tibetan Plateau. Int. Geol. Rev. 55, 958–975.
Jiang, Y.H., Jia, R.Y., Liu, Z., Liao, S.Y., Zhao, P., Zhou, Q., 2013. Origin of middle Triassic high-K calc-alkaline granitoids and their potassic microgranular enclaves from the western Kunlun orogen, northwest China: a record of the closure of Paleo-Tethys. Lithos 156-159, 13–30.
Jiang, C.F., Yang, J.S., Feng, B.G., Zhu, Z., 1992. Opening and Closing Tectonics of the Kunlun Mountains. Geological Publishing House, Beijing (217pp.) (in Chinese).
Johnson, C.M., Beard, B.L., Beukes, N.J., Klein, C., O'Leary, J.M., 2003. Ancient geochemical cycling in the earth as inferred from Fe isotope studies of banded iron formations from the Transvaal craton. Contrib. Mineral. Petrol. 144, 523–547.
Johnson, C.M., Beard, B.L., Klein, C., Beukes, N.J., Roden, E.E., 2008. Iron isotopes constrain biologic and abiologic processes in banded iron formation genesis. Geochim. Cosmochim. Acta 72, 151–169.
Johnson, C.M., Roden, E.E., Welch, S.A., Beard, B.L., 2005. Experimental constraints on Fe isotope fractionation during magnetite and Fe carbonate formation coupled to dissimilatory hydrous ferric oxide reduction. Geochim. Cosmochim. Acta 69, 963–993.
Kasting, J.F., 1993. Earth's early atmosphere. Science 259, 920–926.
Kasting, J.F., 2001. Earth history—the rise of atmospheric oxygen. Science 293, 819–820.
Kimberley, M.M., 1989. Exhalative origins of iron formations. Ore Geol. Rev. 5, 13–145.
Li, N., Chen, Y.J., Santosh, M., Pirajno, F., 2015. Compositional polarity of Triassic granitoids in the Qinling Orogen, China: Implication for termination of the northernmost paleo-Tethys. Gondwana Res. 27, 244–257.
Li, W.Q., Huberty, J.M., Beard, B.L., Kita, N.T., Valley, J.W., Johnson, C.M., 2013. Contrasting behavior of oxygen and iron isotopes in banded iron formations revealed by in situ isotopic analysis. Earth Planet. Sci. Lett. 384, 132–143.
Li, H., Zhang, Z., Li, L., Zhang, Z., Chen, J., Yao, T., 2014. Types and general characteristics of the BIF-related iron deposits in China. Ore Geol. Rev. 57, 264–287.
Liao, S.Y., Jiang, Y.H., Jiang, S.Y., Yang, W.Z., Zhou, Q., Jin, G.D., Zhao, P., 2010. Subducting sediment-derived arc granitoids: evidence from the Datong pluton and its quenched enclaves in the western Kunlun orogen, northwest China. Mineral. Petrol. 100, 55–74.
Lin, S.K., 2015. Study on Geochemistry and Zirocn U–Pb Ages of Dacite Porphyry from the Zankan Iron Deposit, West Kunlun Area Master Thesis Kunming University of Science and Technology, Kunming (64pp.) (in Chinese with English abstract).
Liu, Y., Hu, Z., Gao, S., Günther, D., Xu, J., Gao, C., Chen, H., 2008. In situ analysis of major and trace elements of anhydrous minerals by LA-ICP-MS without applying an internal standard. Chem. Geol. 257, 34–43.
Lyons, T.W., Reinhard, C.T., Planavsky, N.J., 2014. The rise of oxygen in Earth's early ocean and atmosphere. Nature 56, 307–315.
Malinovsky, D., Stenberg, A., Rodushkin, I., Henrik, A., Johan, I., Öhlander, B., Baxter, D.C., 2003. Performance of high resolution MC-ICP-MS for Fe isotope ratio measurements in sedimentary geological materials. J. Anal. At. Spectrom. 18, 687–695.
Mao, S.D., Chen, Y.J., Zhou, Z.J., Lu, Y.H., Guo, J.H., Qin, Y., Yu, J.Y., 2014. Zircon geochronology and Hf isotope geochemistry of the granitoids in the Yangshan gold field, western Qinling, China: implications for petrogenesis, ore genesis and tectonic setting. Geol. J. 49, 359–382.
Matthews, A., Morgans-Bell, H.S., Emmanuel, S., Jenkyns, H.C., Eral, Y., Halicz, L., 2004. Controls on iron-isotope fractionation in organic-rich sediments (Kimmeridge Clay, Upper Jurassic, southern England). Geochim. Cosmochim. Acta 68, 3107–3123.
Mendes, M., Lobato, L.M., Kunzmann, M., Halverson, G.P., 2016. Iron isotope and REE + Y composition of the Cauê banded iron formation and related iron ores of the Quadrilátero Ferrífero, Brazil. Mineral. Deposita. http://dx.doi.org/10.1007/s00126-016-0649-9.
Mi, M., Chen, Y.J., Yang, Y.F., Wang, P., Xu, Y.L., Li, F.L., Wan, S.Q., 2015. Geochronology and geochemistry of the giant Qian'echong Mo deposit, Dabie Shan, eastern China: implications for ore genesis and tectonic setting. Gondwana Res. 27, 1217–1235.
Müller, B., Axelsson, M.D., Öhlander, B., 2003. Trace elements in magnetite from Kiruna, northern Sweden, as determined by LA-ICP-MS. GFF 125, 1–5.
Nadoll, P., Angerer, T., Mauk, J.L., French, D., Walshe, J., 2014. The chemistry of hydrothermal magnetite: a review. Ore Geol. Rev. 61, 1–32.
Nadoll, P., Mauk, J.L., Hayes, T.S., Koenig, A.E., Box, S.E., 2012. Geochemistry of magnetite from hydrothermal ore deposits and host rocks of the Mesoproterozoic Belt Supergroup, United States. Econ. Geol. 107, 1275–1292.
Neilson, R., 2003. Trace Element Partitioning. (http://earthref.org/GERM/tolls/tep.htm).
Nielsen, R.L., Forsythe, L.M., Gallahan, W.E., Fisk, M.R., 1994. Major- and trace-element magnetite-melt equilibria. Chem. Geol. 117, 167–191.

Nishizawa, M., Yamamoto, H., Ueno, Y., Tsuruoka, S., Shibuya, T., Sawaki, Y., Yamamoto, S., Kon, Y., Kitajima, K., Komiya, T., Maruyama, S., Hirata, T., 2010. Grain-scale iron isotopic analysis of pyrite from Precambrian shallow marinecarbonate by femtosecond laser ablation multi-collector ICP–MS technique:new evidence for the redox fluctuation of the Archean shallow ocean. Geochim. Cosmochim. Acta 74, 2760–2778.

Pan, Y.S., Wang, Y., 1994. Tectonic evolution along the geotraverse from Yecheng to Shiquanhe. Acta Geol. Sin. 68, 295–307 (in Chinese with English abstract).

Pan, G.T., Wang, L.Q., Li, X.Z., Wang, J.M., Xu, Q., 2001. The tectonic framework and spatial allocation of the archipelagic arc-basin systems on the Qinghai–Xizang Plateau. Sediment. Geol. Tethyan Geol. 21, 1–26 (in Chinese with English abstract).

Peter, J.M., 2003. Ancient iron-rich metalliferous sediments (iron formations): their genesis and use in the exploration for stratiform base metal sulphide deposits, with examples from the Bathurst Mining Camp. In: Lentz, D.R. (Ed.), Geochemistry of Sediments and Sedimentary Rocks: Evolutionary Considerations to Mineral Deposit Forming Environments. GEOtext 4. Geological Association of Canada, pp. 145–173.

Peter, J.M., Goodfellow, W.D., 1996. Mineralogy, bulk and rare earth element geochemistry of massive sulphide-associated hydrothermal sediments of the Brunswick Horizon, Bathurst mining camp, New Brunswick. Can. J. Earth Sci. 33, 252–283.

Peter, J.M., Goodfellow, W.D., 2003. Hydrothermal sedimentary rocks of the Heath Steele Belt, Bathurst mining camp, New Brunswick. Part 3. Application of mineralogy and mineral and bulk compositions to massive sulfide exploration. Econ. Geol. Monogr. 11, 317–433.

Planaavsky, N., Rouxel, O.J., Bekker, A., Hofmann, A., Little, C.T.S., Lyons, T.W., 2012. Iron isotope composition of some Archean and Proterozoic iron formations. Geochim. Cosmochim. Acta 71, 3833–3846.

Polyakov, V.B., 1997. Equilibrium fractionation of the iron isotopes: estimation from Mössbauer spectroscopy data. Geochim. Cosmochim. Acta 61, 4213–4217.

Polyakov, V.B., Mineev, S.D., 2000. The use of Mössbauer spectroscopy in stable isotope geochemistry. Geochim. Cosmochim. Acta 64, 849–865.

Polyakov, V.B., Clayton, R.N., Horita, J., Mineev, S.D., 2007. Equilibrium iron isotope fractionation factors of minerals: reevaluation from the data of nuclear inelastic resonant X-ray scattering and Mössbauer spectroscopy. Geochim. Cosmochim. Acta 80, 158–169.

Qian, B., Gao, Y.B., Li, K., Zhang, Z.W., Hao, Y.H., 2014. Mineralogy and genesis of the Zankan iron deposit in Taxkorgan area' Xinjiang. Geol. Explor. 50, 630–640 in Chinese with English abstract.

Ren, G.L., Li, J.Q., Wang, H., Liu, J.P., Gao, T., Yang, M., Yi, H., Han, H.H., Yang, J.L., 2013. The metallogenic series of iron deposits in Bulunkou-Zankan, west Kunlun. Xinjiang Geol. 31, 318–323 in Chinese with English abstract.

Rickard, D., 1997. Kinetics of pyrite formation by the H_2S oxidation of iron (II) monosulfide in aqueous solutions between 25 and 125 °C: the rate equation. Geochim. Cosmochim. Acta 61, 115–134.

Rickard, D., Luther, G.W., 1997. Kinetics of pyrite formation by the oxidation of iron (II) monosulphide in aqueous solutions between 25 and 125 °C: the mechanism. Geochim. Cosmochim. Acta 61, 135–147.

Ridler, R.H., 1971. Analysis of Archean volcanic basins in the Canadian Shield using the exhalite concept [abs.]. Bull. Can. Ins. Min. Metall. vol. 64 (no. 714), 20.

Rouxel, O.J., Bekker, A., Edwards, K., 2005. Iron isotope constraints on the Archean and Paleoproterozoic ocean redox state. Science 307, 1088–1091.

Rouxel, O., Dobbek, N., Ludden, J., Fouquet, Y., 2003. Iron isotope fractionation during oceanic crust alteration. Chem. Geol. 202, 155–182.

Rouxel, O., Shanks III, W.C., Bach, W., Edwards, K.J., 2008. Integrated Fe- and S-isotope study of seafloor hydrothermal vents at East Pacific rise 9–10°N. Chem. Geol. 252, 214–227.

Rudnick, R.L., Gao, S., 2003. Composition of the continental crust. In: Holland, H.D., Turekian, K.K. (Eds.), Treatise on Geochemistry. Elsevier-Pergaman, Oxford, pp. 1–64.

Rusk, B.G., Oliver, N., Brown, A., Lilly, R., Jungmann, D., 2009. Barrenmagnetite breccias in the Cloncurry region, Australia; comparisons to IOCG deposits. Smart science for exploration andmining. Proceedings of the 10th Biennial Society for Geology Applied to Mineral Deposits (SGA) Meeting. Townsville, pp. 656–658.

Sadler, P.M., 1981. Sediment accumulation rates and the completeness of stratigraphic sections. J. Geol. 89, 569–584.

Sangster, D.F., 1978. Exhalites associated with Archaean volcanogenic massive sulphide deposits. 2. University of Western Australia. Geology Department and Extension Service Publication, pp. 70–81.

Schoonen, M.A.A., Barnes, H.L., 1991. Reactions forming pyrite and marcasite from solution: III. Hydrothermal processes. Geochim. Cosmochim. Acta 55, 3491–3504.

Seto, M., Kitao, S., Kobayashi, Y., Haruki, R., Yoda, Y., Mitsui, T., Ishikawa, T., 2003. Site-specific phonon density of states discerned using electronic states. Phys. Rev. Lett. 91, 185505-1–185505-4.

Severmann, S., Johnson, C.M., Beard, B.L., German, C.R., Edmonds, H.N., Chiba, H., Green, D.R.H., 2004. The effect of plume processes on the Fe isotope compositionof hydrothermally derived Fe in the deep ocean as inferred from the Rainbowvent site, mid-Atlantic ridge, 36°14′N. Earth Planet. Sci. Lett. 225, 63–76.

Severmann, S., Johnson, C.M., Beard, B.L., McManus, J., 2006. The effect of early dia-genesis on the Fe isotope compositions of porewaters and authigenic mineralsin continental margin sediments. Geochim. Cosmochim. Acta 70, 2006–2022.

Sharma, M., Polizzotto, M., Anbar, A.D., 2001. Iron isotopes in hot springs along theJuan de Fuca ridge. Earth Planet. Sci. Lett. 194, 39–51.

Simon, A.C., Candela, P.A., Piccoli, P.M., Mengason, M., Englander, L., 2008. The effect of crystal–melt partitioning on the budgets of Cu, Au, and Ag. Am. Mineral. 93, 1437–1448.

Simonson, B.M., 2003. Origin and evolution of large Precambrian iron formations. Geol. Soc. Am. Spec. Pap. 370, 231–244.

Singoyi, B., Danyushevsky, L., Davidson, G.J., Large, R., Zaw, K., 2006. Determination of trace elements in magnetites from hydrothermal deposits using the LA ICP-MS technique. SEG Keystone Conference. CD-ROM, Denver, USA.

Slack, J.F., Shanks III, W.C., 2012. Exhalites. In: Thurston, R. (Ed.), Volcanogenic Massive Sulfide Occurrence Model, pp. 157–163 (Scientific Investigations Report 2010-5070-C).

Slack, J.F., Grenne, T., Bekker, A., 2009. Seafloor-hydrothermal Si–Fe–Mn exhalites in the Pecos greenstone belt, New Mexico, and the redox state of ca. 1720 Ma deep seawater. Geosphere 5, 302–314.

Spry, P.G., Peter, J.M., Slack, J.F., 2000. Meta-exhalites as exploration guides to ore. In: Spry, P.G., Marshall, B., Vokes, F.M. (Eds.), Metamorphosed and Metamorphic Ore Deposits. 11, pp. 163–201 (Rev. Econ. Geol.).

Steinhoefel, G., von Blanckenburg, F., Horn, I., Konhauser, K.O., Beukes, N.J., Gutzmer, J., 2010. Deciphering formation processes of banded iron formations from the Transvaal and the Hamersley successions by combined Si and Fe isotope analysis using UV femtosecond laser ablation. Geochim. Cosmochim. Acta 74, 2677–2696.

Sun, H.T., Li, C.J., Wu, H., Wang, H.J., Qi, S.J., Chen, G.M., Liu, Z.T., Gao, P., 2003. Overview of Metallogenesis on Western Kunlun. Geological Publishing House, Beijing (251pp.) (in Chinese).

Sun, J., Zhu, X.K., Chen, Y.L., Fang, N., 2013. Iron isotopic constraints on the genesis of Bayan Obo ore deposit, Inner Mongolia, China. Precambrian Res. 235, 88–106.

Sun, X.H., Zhu, X.Q., Tang, H.S., Zhang, Q., Luo, T.Y., 2014. The Gongchangling BIFs from the Anshan–Benxi area, NE China: petrological–geochemical characteristics and genesis of high-grade iron ores. Ore Geol. Rev. 63 (3), 374–387.

Tang, H.S., Chen, Y.J., 2013. Global glaciations and atmospheric change at ca. 2.3 Ga. Geosci. Front. 4, 583–596.

Teitler, Y., Duuring, P., Hagemann, S.G., 2014. Styles and controls of BIF-hosted iron ore in Archean terranes, comparison between the Pilbara and Yilgarn Cratons. 2014. Australian Earth Sciences Convention (AESC), Newcastle.

Toplis, M.J., Carroll, M.R., 1995. An experimental study of the influence of oxygen fugacity on Fe–Ti oxide stability, phase relations, and mineral-melt equilibria in ferro-basaltic systems. J. Petrol. 36, 1137–1170.

Toplis, M.J., Corgne, A., 2002. An experimental study of element partitioning between magnetite, clinopyroxene and iron-bearing silicate liquids with particular emphasis on vanadium. Contrib. Mineral. Petrol. 144, 22–37.

Van Baalen, M.R., 1993. Titaniummobility inmetamorphic systems: a review. Chem. Geol. 110, 233–249.

Verlaguet, A., Brunet, F., Goffé, B., Murphy, W.M., 2006. Experimental study and modeling of fluid reaction paths in the quartz–kyanite ± muscovite–water system at 0.7 GPa in the 350–550 °C range: implications for Al selective transfer during metamorphism. Geochim. Cosmochim. Acta 70, 1772–1788.

Wang, P., Chen, Y.J., Fu, B., Yang, Y.F., Mi, M., Li, Z.L., 2014. Fluid inclusion and H-O-C isotope geochemistry of the Yaochong porphyry Mo deposit in Dabie Shan, China: A case study of porphyry systems in continental collision orogens. Int. J. Earth Sci. 103, 777–797.

Whitehouse, M.J., Fedo, C.M., 2007. Microscale heterogeneity of Fe isotopes in >3.71 Ga banded iron formation from the Isua greenstone belt, southwest Greenland. Geology 35, 719–722.

Xiao, X.C., Jun, W., Li, S.U., Ji, W.H., Song, S.G., 2005b. An early aged ophiolite in the western Kunlun Mts., NW Tibetan plateau and its tectonic implications. Acta Geol. Sin. 79, 778–786.

Xiao, W.J., Windley, B.F., Liu, D.Y., Jian, P., Liu, C.Z., Yuan, C., Sun, M., 2005a. Accretionary tectonics of the Western Kunlun Orogen, China: a Paleozoic-early Mesozoic, long-lived active continentalmargin with implications for the growth of southern Eurasia. J. Geol. 113, 687–705.

Xiao, W.J., Hou, Q.L., Li, J.L., 2000. Tectonic facies and the archipelago-accretion process of the west Kunlun. China. Sci. China Ser. D 43, 134–143 (supp.).

Xu, R.H., Zhang, Y.Q., Xie, Y.W., Chen, F.K., Vadal, P., Nicolas, A., Zhang, Q.D., Zhao, D.M., 1994. A discovery of an early Palaeozoic tectonomagmatic belt in the northern part of west Kunlun mountains. Sci. Geol. Sin. 4, 313–328 in Chinese with English abstract.

Yan, C.H., Cao, X.Z., Zhang, W.S., Chen, J.K., Liu, B.D., Wang, S.Y., Zhang, S.B., Li, S.P., Liu, S.J., 2012a. The "Pamir-Type" Iron Deposits. Geological Publishing House, Beijing (256pp.) (in Chinese).

Yan, C.H., Chen, C.J., Cao, X.Z., Zhang, W.S., Chen, J.K., Li, S.P., Liu, P.D., 2012b. The discovery of the "Pamir-type" iron deposits in Taxkorgan area of Xinjiang and its geological significance. Geol. Bull. China 31, 549–557 in Chinese with English abstract.

Yang, W.Q., 2013. The Indosinian metamorphism, magmatism and formation age of Bunlunkuole rock group in Taxkorgan-Kangxiwa tectonic belt, Western Kunlun Ph.D. Thesis Northwest University, Xian (128pp.) (in Chinese with English abstract).

Yang, W.Q., Liu, L., Cao, Y.T., Wang, C., He, S.P., Li, R.S., Zhu, X.H., 2010. Geochronological evidence of Indosinian (high-pressure) metamorphic event and its tectonic significance in Taxkorgan area of the western Kunlun Mountains, NW China. Sci. China Earth Sci. 53, 1445–1459.

Yoshiya, K., Nishizawa, M., Sawaki, Y., Ueno, Y., Komiya, T., Yamada, K., Yoshida, N., Hirata, T., Wada, H., Maruyama, S., 2012. In situ iron isotope analyses of pyrites and organic carbon isotope ratios in the Fortescue group: metabolic variation of a late Archean ecosystem. Precambrian Res. 212–213, 169–193.

Zhang, C.L., Lu, S.N., Yu, H.F., Ye, H.M., 2007. Tectonic evolution of western orogenic belt: evidences from zircon SHRIMP and LA–ICP–MS U–Pb ages. Sci. China Ser. D Earth Sci. 37, 145–154.

Zheng, Z., Deng, X.H., Chen, H.J., Yue, S.W., Dong, L.H., Qu, X., Chen, Y.J., 2016. Fluid sources and metallogenesis in the Baiganhu W-Sn deposit, East Kunlun, NW China: insights from chemical and boron isotopic compositions of tourmaline. Ore Geol. Rev. 72, 1129–1142.

Zhou, Z.J., Chen, Y.J., Jiang, S.Y., Zhao, H.X., Qin, Y., Hu, C.J., 2014a. Geology, geochemistry and ore genesis of the Wenyu gold deposit, Xiaoqinling gold field, southern margin of North China craton. Ore Geol. Rev. 59, 1–20.

Zhou, Z.J., Liu, Z.W., Qin, Y., 2014b. Geology, geochemistry and genesis of the Huachanggou gold deposit, western Qinling Orogen, central China. Geol. J. 49, 424–441.

Zhou, Z.J., Chen, Y.J., Jiang, S.Y., Hu, C.J., Qin, Y., Zhao, H.X., 2015. Isotope and fluid inclusion geochemistry and ore genesis of the Qiangma gold deposit, Xiaoqinling gold field, Qinling Orogen, southern margin of North China Craton. Ore Geol. Rev. 66, 47–64.

Zhou, Z.J., Mao, S.D., Chen, Y.J., Santosh, M., 2016. U-Pb ages and Lu-Hf isotopes of detrital zircons from the southern Qinling Orogen: implications for Precambrian to Phanerozoic tectonics in central China. Gondwana Res. 35, 323–337.

Zhu, X.K., Guo, Y., O'Nions, R.K., Young, E.D., Ash, R.D., 2001. Isotopic homogeneity of iron in the early solar nebula. Nature 412, 311–313.

Zhu, X.K., O'Nions, R.K., Guo, Y.C., Reynolds, B.C., 2000. Secular variation of iron isotopes in North Atlantic Deep Water. Science 287, 2000–2002.

Zhu, X.Q., Tang, H.S., Sun, X.H., 2014. Genesis of banded iron formations: a series of experimental simulations. Ore Geol. Rev. 63, 465–469.